

NONLINEAR AEROELASTIC ANALYSIS OF  
HIGH ASPECT-RATIO WINGS  
USING THE METHOD OF NUMERICAL CONTINUATION

A Thesis

by

CHETAN NICHKAWDE

Submitted to the Office of Graduate Studies of  
Texas A&M University  
in partial fulfillment of the requirements for the degree of  
MASTER OF SCIENCE

May 2006

Major Subject: Aerospace Engineering

NONLINEAR AEROELASTIC ANALYSIS OF  
HIGH ASPECT-RATIO WINGS  
USING THE METHOD OF NUMERICAL CONTINUATION

A Thesis

by

CHETAN NICHKAWDE

Submitted to the Office of Graduate Studies of  
Texas A&M University  
in partial fulfillment of the requirements for the degree of

MASTER OF SCIENCE

Approved by:

Chair of Committee, Thomas W. Strganac  
Committee Members, John E. Hurtado  
Alan Palazzolo

Head of Department, Walter E. Haisler

May 2006

Major Subject: Aerospace Engineering

## ABSTRACT

Nonlinear Aeroelastic Analysis of High Aspect-Ratio Wings

Using the Method of Numerical Continuation. (May 2006)

Chetan Nickkawde, B.Tech., Indian Institute of Technology Bombay;

M.Tech., Indian Institute of Technology Bombay

Chair of Advisory Committee: Dr. Thomas W. Strganac

This research explores the impact of kinematic structural nonlinearities on the dynamics of a highly deformable cantilevered wing. Two different theoretical formulations are presented and analysed for nonlinear behavior. The first formulation, which is more conventional, assumes zero equilibria and structural nonlinearities occur as terms up to third order in the Taylor series expansion of structural nonlinearities. In the second approach, no prior assumption about equilibria states of the wing is made. Kinematic nonlinearities due to curvature and inertia were retained in their exact form. Thus, the former becomes a special case of the latter. This nonlinear formulation permits the analysis of dynamics about nonzero trims. Nonzero trim states are computed as a system parameter is varied using a continuation software tool. The stability characteristics of these trim states are also ascertained. Various bifurcation points of the system are determined. Limit-cycle oscillations are also investigated for and are characterized in terms of amplitude of vibration. The research in particular examines the impact of in-plane degree of freedom on the stability of nonzero trim states. The effect of variation of system parameters such as stiffness ratio, aspect ratio and root angle of attack is also studied. The method of direct eigenanalysis of nonzero equilibria is novel and new for an aeroelastic system.

To my beloved parents and almighty God

## ACKNOWLEDGMENTS

I take this opportunity to extend my gratitude and deep appreciation for my adviser Dr. Thomas Strganac for his keen involvement and invaluable advice during the course of the work. He has been very patient and considerate. I extend my sincere thanks to Air Force Office Scientific Research (AFOSR) for funding my work.

My friends Dhananjay and Tirtharaj have been my tennis and swimming mates during my stay here in College Station. I would also like to thank them for many of our adventure road trips in Texas and beyond. I would like to thank my parents for their constant support and encouragement.

Last but not the least, I would like to thank God for providing me steadiness, determination and confidence to overcome obstacles.

## TABLE OF CONTENTS

CHAPTER		Page
I	INTRODUCTION . . . . .	1
II	FORMULATION I: BENDING-BENDING-TORSION DY- NAMICS ABOUT ZERO EQUILIBRIA . . . . .	5
	A. Equations of Motion . . . . .	5
	B. Solution Procedure . . . . .	12
	C. Validation of Code . . . . .	16
	D. Evaluation of System Dynamics . . . . .	17
	E. Internal Resonance . . . . .	23
III	FORMULATION II: THREE DIMENSIONAL MOTION ABOUT NONZERO EQUILIBRIA . . . . .	29
	A. Physical Model . . . . .	31
	1. Aerodynamics . . . . .	37
	B. Dynamics about Nonzero Equilibria . . . . .	38
	1. Stiffness Ratio Effect . . . . .	40
	2. Subcritical Hopf Bifurcation . . . . .	41
IV	CONCLUSIONS . . . . .	50
	REFERENCES . . . . .	51
	APPENDIX A . . . . .	54
	VITA . . . . .	57

## LIST OF TABLES

TABLE		Page
I	Baseline values of the parameters for NATA wing . . . . .	20
II	Baseline values of the parameters for the heavy Golland wing[17] . . .	24
III	Baseline values of the parameters for the extended heavy Golland wing	38
IV	Subcritical bifurcation . . . . .	41

## LIST OF FIGURES

FIGURE	Page
1	Design and performance analysis requirements of new UAV concepts exceed current capabilities . . . . . 2
2	Subcritical Hopf-type bifurcations yield LCO states for $V < V_{Flutter}$ . 3
3	Wing showing local and global coordinate system . . . . . 6
4	Verification of code: Out-of-plane and torsion free response of heavy Goland wing illustrating matching time period of motion . . . 17
5	Validation of code: $V=100$ ft/sec, heavy Goland wing with linear structure and linear aerodynamics; initial condition: $(v, \phi, \dot{v}, \dot{\phi}) = (0.05, 0.03, 0, 0)$ . . . . . 18
6	Time response of heavy Goland wing at $V=210$ ft/sec; initial condition: $(v, \phi, \dot{v}, \dot{\phi}) = (0.05, 0.03, 0, 0)$ . . . . . 19
7	Comparison of bifurcation diagrams with $(\beta_\eta - 1)v''^2\phi$ retained(left view) and removed(right view) . . . . . 21
8	Bifurcation diagram with term $(\beta_\eta - 1)(v''\phi)''$ and $(\beta_\eta - 1)(v''w'')$ removed . . . . . 22
9	Bifurcation diagram for system with $\beta_\eta = 2$ (left view) and $\beta_\eta = 44$ (right view); all nonlinear terms retained . . . . . 23
10	Bifurcation diagram with $L$ as parameter . . . . . 26
11	Bifurcation diagram at $V = 108$ ft/sec illustrating internal resonance . . . . . 26
12	Simulation illustrating internal resonance (heavy Goland wing, $V = 108$ ft/sec, $L = 38$ ft and $\beta_\eta = 44$ ) . . . . . 27
13	Locus of Hopf bifurcation in $V$ - $L$ parameter space . . . . . 27



FIGURE	Page
14	Bifurcation diagram at $V = 107$ ft/sec showing absence of resonance . . . . . 28
15	Velocity-Length internal resonance pair . . . . . 28
16	Airfoil section showing the lift resolved in $(x, y, z)$ coordinate system . . . . . 43
17	Bifurcation diagram with $V$ as the parameter showing the out-of-plane bending modal coordinate for the heavy Goland wing with $L=100$ , $\beta_\eta = 144$ for two different root angles of attack, $\alpha_0$ . . . . . 43
18	Simulation result at $V=70$ ft/s for two different root angles of attack . . . . . 44
19	Locus of Hopf bifurcation in $V$ - $\beta_\eta$ parameter space for various values of $\alpha_0$ . . . . . 45
20	Bifurcation diagram with $V$ as the parameter showing the in-plane bending modal coordinate for the heavy Goland wing with $L=100$ , $\alpha_0 = 2.8^\circ$ for two different stiffness ratios, $\beta_\eta$ . . . . . 46
21	Locus of eigenvalues for different values of stiffness ratio . . . . . 46
22	Comparison of bifurcation diagrams with $V$ as the parameter showing the out-of-plane bending modal coordinate for the heavy Goland wing with $\beta_\eta = 25$ , $L = 100$ and $\alpha_0 = 2.8^\circ$ . . . . . 47
23	Comparison of bifurcation diagrams with $V$ as the parameter showing the out-of-plane bending modal coordinate for the heavy Goland wing with $L = 100$ and $\alpha_0 = 5.6^\circ$ . . . . . 47
24	Comparison of bifurcation diagrams with $V$ as the parameter showing the in-plane bending modal coordinate for the heavy Goland wing with $L = 100$ and $\alpha_0 = 5.6^\circ$ . . . . . 48
25	Out-of-plane bending response and two different initial conditions for $V = 140$ ft/sec, $\beta_\eta = 25$ , $L = 100$ feet and $\alpha_0 = 2.8^\circ$ . . . . . 48
26	In-plane bending response and two different initial conditions for $V = 140$ ft/sec, $\beta_\eta = 25$ , $L = 100$ feet and $\alpha_0 = 2.8^\circ$ . . . . . 49
27	Comparison of bifurcation diagrams with $V$ as the parameter showing the out-of-plane bending modal coordinate with $\beta_\eta = 4$ and $\alpha_0 = 2.8^\circ$ . . . . . 49

## NOMENCLATURE

$AR$	aspect ratio
$D$	stiffness
$e$	cg offset from elastic axis
$g$	acceleration due to gravity
$I$	moment of inertia
$L$	wing semispan
$m$	mass per length
$M_0$	body mass
$q$	dynamic pressure
$V$	freestream velocity
$V_y$	vertical velocity
$v$	out-of-plane displacement
$w$	in-plane displacement
$\alpha_0$	root angle of attack
$\beta_\eta$	in-plane stiffness ratio
$\beta_\phi$	torsion stiffness ratio
$\omega$	angular velocity
$\phi$	torsion displacement
$\psi$	$z$ -rotation Euler angle
$\rho$	bending curvature
$\theta$	$y$ -rotation Euler angle
<i>Subscripts</i>	
$\eta$	about $\eta$ axis
$\xi$	about $\xi$ axis
$\zeta$	about $\zeta$ axis

## CHAPTER I

## INTRODUCTION

Performance requirements of future air vehicles, such as endurance, autonomous behavior, mobility, payload requirements, and vehicle size, drive designs that well exceed our present capabilities to accurately analyze the behavior of candidate systems. Even existing air vehicles (and pilot performance) are limited by nonlinear behavior that are not understood and which are subjects of current research investigations. The development of new Uninhabited Air Vehicles (UAVs) will require improved understanding of large-amplitude nonlinear interactions, flow physics, and nonlinear and multi-functional structures. Existing analysis and design tools are not suited for analysis of new classes of future aircraft such as SensorCraft UAVs depicted in Fig. 1. The fundamental science issues associated with managing nonlinear aeroelastic effects have not been fully explored in configurations of this scale (200+ feet wingspans with aspect ratios greater than 30). Active wing technologies, such as those explored in the Active Aeroelastic Wing (AAW) program, utilize pronounced twisting and bending to achieve desired aerodynamic loads. For high-aspect ratio wings, major benefits of such active wing technology are shape optimization for lightweight design to improve payload capacity and gust load alleviation.

In recent years, studies of nonlinear fluid-structure interactions have been motivated by evidence that there are adverse aeroelastic responses attributed to system nonlinearities. For example, limit-cycle oscillations (LCOs) occur in nonlinear aeroelastic systems and remain a persistent problem on fighter aircraft with store configurations. Nonlinear phenomena such as LCOs have been observed as reported by

---

The journal model is *IEEE Transactions on Automatic Control*.

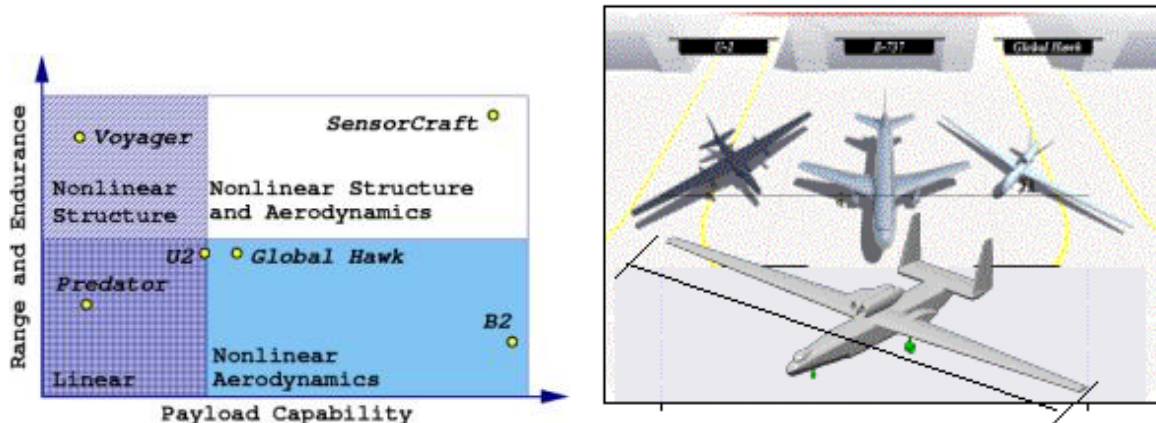


Fig. 1. Design and performance analysis requirements of new UAV concepts exceed current capabilities

Bunton and Denegri[1], and Denegri[2]. Such LCOs are unacceptable since aircraft performance, aircraft certification, mission capability, and human factor issues such as pilot fatigue are adversely affected. Research has improved the understanding of LCO responses that limit vehicle and pilot performance, and such research efforts are relevant to understanding behavior of new air vehicle concepts, including high altitude, long endurance UAVs. Kim and Strganac[3] studied LCOs of a cantilever wing with three possible nonlinearities, including aerodynamic, structural, and store-induced nonlinearities. When these three nonlinearities were combined, LCOs were observed at speeds below the flutter velocity. The presence of subcritical LCOs was dominated by the structural nonlinearity, yet the aerodynamic and store nonlinearities change the characteristic of the nonlinear responses. Kim, Nichkawde and Strganac[4] did bifurcation studies of wing-with-store configuration. The stiffness ratio between in-plane and out-of-plane bending motion was found to be a critical parameter governing nonlinear dynamics. More recently, Beran, Strganac, Kim and Nichkawde[5] presented preliminary studies on an approach to couple nonlinear structural and aerodynamic methods to examine LCOs in the transonic flow regime.

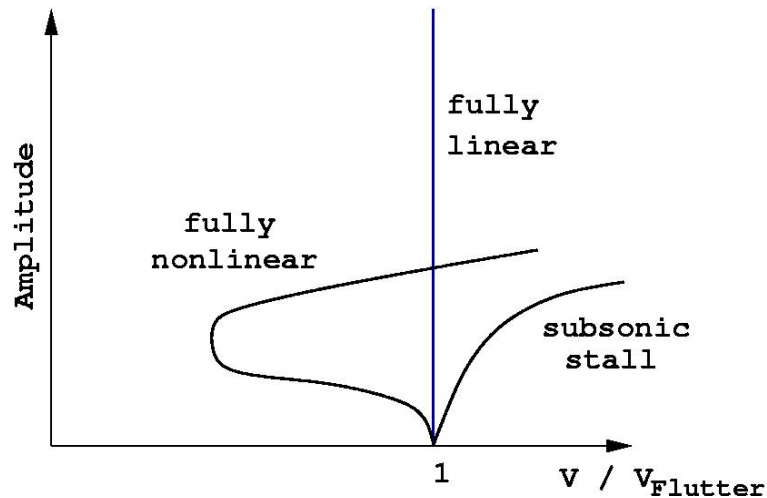


Fig. 2. Subcritical Hopf-type bifurcations yield LCO states for  $V < V_{Flutter}$

This research examines the impact of geometric structural nonlinearities on the dynamics of high aspect ratio flexible wing using a combination numerical continuation tool and time domain simulations. The aerodynamic loads is represented by a quasi-steady aerodynamic model. The nonlinear analyses considers the vast parameter space. Various bifurcation characteristics, unique to the aeroelastic system, have been identified as illustrated in Fig. 2. These include both subcritical and supercritical bifurcations, the nature of which must be examined in detail. The former case is of significant interest because flight test experiences indicate the presence of subcritical Hopf-type bifurcations, in which limit cycle oscillations below the classical flutter boundary. In addition, subcritical bifurcations depend upon the system disturbance, and have a hysteresis between onset and recovery speeds. This sub-flutter behavior cannot be studied with linear methods that are common to today approaches.

A brief outline of the thesis is as follows. In chapter II of the thesis, a nonlinear structural formulation for bending-bending-torsion dynamics of the wing is presented. This formulation has been derived from the work of Crespo Da Silva[6]. The kine-

matic nonlinearities are expressed as Taylor series expansion about zero equilibria and terms up to third order is retained. The formulation is similar to one used by Kim et al[7]. A continuation tool is applied to this formulation and the effect structural nonlinearities on the bifurcation characteristics is investigated. The third chapter presents a set of geometrically exact nonlinear formulation of cantilever wing. However, here no prior assumption about equilibria state of the wing is made. Thus, no Taylor series expansion is performed and the nonlinearities are retained in their exact form. Thus, this model permits examination of nonzero equilibria states and their stability characteristics. Parametric studies is performed using a continuation tool. The fourth and last chapter concludes this thesis by summarizing the findings of this research.

## CHAPTER II

FORMULATION I: BENDING-BENDING-TORSION DYNAMICS ABOUT ZERO  
EQUILIBRIA

This chapter presents the equations of motion for bending-bending-torsion dynamics of cantilevered wing. The solution procedure is elaborated in detail. The model equations assumes zero equilibria. The ordinary differential equations obtained via Galerkin procedure are coded in AUTO2000, which is a continuation and bifurcation software. Bifurcation analysis is performed. Term by term sensitivity of structural nonlinearities is done. Bifurcation analysis also reveals possible internal resonance for the aeroelastic system.

## A. Equations of Motion

The nonlinear equations of motion for a cantilever wing are derived from the equations of motion for flexural-flexural-torsional vibrations. The formulation follows an approach developed by Crespo da Silva[6] but includes mass imbalances. The equations contain structural coupling terms and include both quadratic and cubic nonlinearities due to curvature and inertia. Longitudinal extension is not permitted; thus, the equations are derived with an inextensionality constraints along the span.

A beam segment of length  $s$  is shown in Fig. 3. The axes  $(x, y, z)$  are assumed to be fixed in the inertial frame, while  $(\xi, \eta, \zeta)$  are taken to be the principal axes of the beam cross-section at position  $s$ . This axes system is arbitrarily oriented in space with respect to the inertial axes system. The orientation of the  $(\xi, \eta, \zeta)$  system with respect to the  $(x, y, z)$  frame is described by the set of 3-2-1 Euler angles  $\psi(s, t)$ ,  $\theta(s, t)$  and  $\phi(s, t)$ . The beam is assumed to be inextensional lengthwise. This constraint can

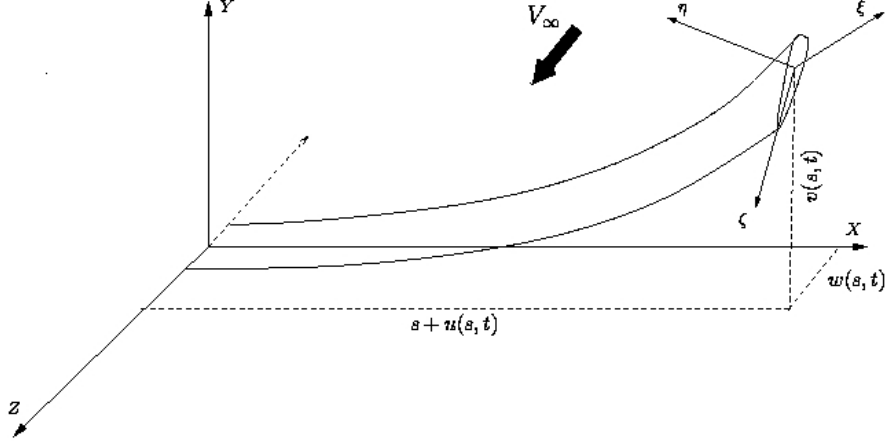


Fig. 3. Wing showing local and global coordinate system

be expressed mathematically:

$$(1 + u')^2 + v'^2 + w'^2 = 1 \quad (2.1)$$

The above constraint, although artificial, is a valid approximation if the extensional stiffness of the wing is large.

The governing equations for bending-bending-torsion dynamics of a cantilevered wing with associated boundary conditions were derived by Crespo da Silva et al [6]. The possibility of mass offset was not taken into account[6]. The linear contribution due to the presence of mass offset was added to the equation by Kim[7]. Thus, the equations of motion for in-plane bending ( $w$ ), out-of-plane ( $v$ ), and torsion ( $\phi$ )



response are

$$\begin{aligned}
m\ddot{w} - I_\eta \ddot{w}'' + D_\eta w^{IV} &= G'_w + qbC_A \\
m\ddot{v} - me\ddot{\phi} - I_\zeta \ddot{v}'' + D_\zeta v^{IV} &= G'_v + qbC_N \\
I_\xi \ddot{\phi} - me\ddot{v} - D_\xi \phi'' &= G_\phi + qb^2C_M
\end{aligned} \tag{2.2}$$

In the above equations, linear terms are written on the left-hand side and the corresponding nonlinear terms are simply expressed by  $G'_w$ ,  $G'_v$ , and  $G_\phi$ .  $C_A$  and  $C_N$  are axial and normal aerodynamic force coefficients and  $C_M$  is the aerodynamic moment coefficient about the elastic axis. Quasi-steady aerodynamic formulation is used to obtain aerodynamic forces. The nonlinear structural terms are expanded with a Taylor series expansion about the static undeformed wing configuration. Terms up to third order are retained in the final expression. Higher order nonlinearities are neglected assuming they would have negligible effect on the system dynamics. The nonlinear components are defined as

$$\begin{aligned}
G'_w &= \{D_\xi (\phi' + v''w') v'' - [(D_\eta - D_\zeta) (\phi v'' + \phi^2 w'')]'\} \\
&\quad - w' (D_\zeta v''^2 + D_\eta w''^2) - I_\xi (\dot{\phi} + \dot{v}'w') \dot{v}' - [(I_\eta - I_\zeta) (\phi \dot{v}' + \phi^2 \dot{w}')]^\bullet \\
&\quad + w' (I_\zeta \dot{v}'^2 + I_\eta \dot{w}'^2) + \lambda w'\} \tag{2.3}
\end{aligned}$$

$$\begin{aligned}
G'_v &= \{-D_\xi (\phi' + v''w') w'' - [(D_\eta - D_\zeta) (\phi^2 v'' - \phi w'' - v'w'w'')]'\} \\
&\quad - v' (D_\zeta v''^2 + D_\eta w''^2) + I_\xi (\dot{\phi} + \dot{v}'w') \dot{w}' + [(I_\eta - I_\zeta) (\phi^2 \dot{v}' - \phi \dot{w}' - v'w'\dot{w}')]^\bullet \\
&\quad + v' (I_\zeta \dot{v}'^2 + I_\eta \dot{w}'^2) + \lambda v' + w' qb^2 C_M\} \tag{2.4}
\end{aligned}$$

$$\begin{aligned}
G_\phi &= D_\xi (w'v'')' - (D_\eta - D_\zeta) [(v''^2 - w''^2)\phi - v''w''] \\
&\quad - I_\xi (w'\dot{v}')^\bullet + (I_\eta - I_\zeta) [(\dot{v}'^2 - \dot{w}'^2)\phi - \dot{v}'\dot{w}'] \tag{2.5}
\end{aligned}$$

The reader is referred to Crespo da Silva et al[6] for details of the development of above nonlinear expressions. The  $\lambda$  in Eqs. (2.3) and (2.4) is the Lagrange multiplier used to append the constraint given by Eq. (3.5) to the Lagrangian and hence needs to be eliminated. In addition to the above three nonlinear components, the nonlinear expression relating  $u$  motion to  $v$ ,  $w$ ,  $\phi$  and the Lagrange multiplier  $\lambda$  is given by

$$\begin{aligned}
G'_u = & \{D_\xi \phi'(w''v' - v''w') - v'[(D_\eta - D_\zeta)\phi w'']' - w'[(D_\eta - D_\zeta)\phi v'']' \\
& + D_\zeta v'v''' + D_\eta w'w''' - I_\xi \dot{\phi}(\dot{w}'v' - \dot{v}'w') \\
& + (I_\eta - I_\zeta)[(\dot{w}'\phi)^\bullet + (\dot{v}'\phi)^\bullet w'] - I_\zeta \ddot{v}'v' - I_\eta \ddot{w}'w' \\
& + \lambda(1 + u') - v'w'qb^2C_M\}' = m\ddot{u} - qbC_u
\end{aligned} \tag{2.6}$$

Above is the governing equation for  $u$ -dynamics which is constrained by Eq. (3.5).  $C_u$  in the above equation is the aerodynamic force coefficient in the  $u$ -direction. Equation (2.6) together with the boundary condition  $G_u(L, t) = 0$  and the inextensionality constraint given by Eq. (3.5) can be used to eliminate  $\lambda$  from the expressions for  $G'_w$  and  $G'_v$ . Only a second order expression for  $\lambda$  is required as nonlinear terms up to only third order are being retained. Thus, integrating Eq. 2.6 from  $L$  to  $x$  yields

$$\int_L^x G'_u dx = \int_L^x (m\ddot{u} - qbC_u) dx \tag{2.7}$$

The inextensionality constraint is approximated as

$$\begin{aligned}
u' &= -\frac{1}{2}(v'^2 + w'^2) \\
\text{or } u &= -\frac{1}{2} \int_0^x (v'^2 + w'^2) d\hat{x}
\end{aligned} \tag{2.8}$$

Thus, after eliminating  $u$  from Eq. (3.28) by using Eq. (2.8)

$$G_u(y, t) = G_u(L, t) - \int_L^x \left( \frac{1}{2}m \left[ \int_0^y (v'^2 + w'^2) d\hat{x} \right]^{\bullet\bullet} + qbC_u \right) dx \tag{2.9}$$

From the natural boundary conditions[6],

$$G_u(L, t) = 0 \quad (2.10)$$

Thus,

$$G_u(y, t) = - \int_L^x \left( \frac{1}{2}m \left[ \int_0^y (v'^2 + w'^2) d\hat{x} \right]^{\bullet\bullet} + qbC_u \right) dx \quad (2.11)$$

Substituting the expression for  $G_u$  and retaining terms up to second order, the expression for  $\lambda$  is obtained as follows

$$\begin{aligned} \lambda = & -D_\zeta v'v''' - D_\eta w'w''' + I_\zeta \ddot{v}'v' + I_\eta \ddot{w}'w' + v'w'qb^2C_M \\ & - \int_L^x \left( \frac{1}{2}m \left[ \int_0^x (v'^2 + w'^2) d\hat{x} \right]^{\bullet\bullet} + qbC_u \right) dx \end{aligned} \quad (2.12)$$

It can be shown that  $\lambda$  is the force tangent to the neutral axis necessary to maintain the inextensionality constraint [8]. Substituting the expression for  $\lambda$  in to Eqs. (2.3) and (2.4), the nonlinear structural contribution can be expressed as

$$\begin{aligned} G'_w = & \{D_\xi (\phi' + v''w') v'' - [(D_\eta - D_\zeta) (\phi v'' + \phi^2 w'')]'\} \\ & - w' (D_\zeta v'^2 + D_\eta w'^2) - I_\xi (\dot{\phi} + \dot{v}'w') \dot{v}' - [(I_\eta - I_\zeta) (\phi \dot{v}' + \phi^2 \dot{w}')]^\bullet \\ & + w' (I_\zeta \dot{v}'^2 + I_\eta \dot{w}'^2) - w' (D_\zeta v'v''' + D_\eta w'w''') + w' (I_\zeta \ddot{v}'v' + I_\eta \ddot{w}'w') \\ & - w' \left[ \int_L^x \left( \frac{1}{2}m \left[ \int_0^x (v'^2 + w'^2) d\hat{x} \right]^{\bullet\bullet} + qbC_u \right) dx \right] + v'w'w'qb^2C_M \} \end{aligned} \quad (2.13)$$

$$\begin{aligned} G'_v = & \{-D_\xi (\phi' + v''w') w'' - [(D_\eta - D_\zeta) (\phi^2 v'' - \phi w'' - v'w'w'')]'\} \\ & - v' (D_\zeta v'^2 + D_\eta w'^2) + I_\xi (\dot{\phi} + \dot{v}'w') \dot{w}' + [(I_\eta - I_\zeta) (\phi^2 \dot{v}' - \phi \dot{w}' - v'w'\dot{w}')]^\bullet \\ & + v' (I_\zeta \dot{v}'^2 + I_\eta \dot{w}'^2) - v' (D_\zeta v'v''' + D_\eta w'w''') + v' (I_\zeta \ddot{v}'v' + I_\eta \ddot{w}'w') \\ & - v' \left[ \int_L^x \left( \frac{1}{2}m \left[ \int_0^x (v'^2 + w'^2) d\hat{x} \right]^{\bullet\bullet} + qbC_u \right) dx \right] \\ & + w'v'v'qb^2C_M + w'qb^2C_M \} \end{aligned} \quad (2.14)$$

It is of value to examine the nondimensional version of these equations. The  $x$  co-ordinate is non-dimensionalized by the wing length,  $L$  and nondimensional co-ordinate  $s$  is defined as follows  $s = \frac{x}{L}$ . Thus, the spatial derivative can be expressed as follows

$$\frac{\partial}{\partial x^k} = \frac{1}{L^k} \frac{\partial}{\partial s^k}, \quad k \in N$$

The parameter  $L$  can be expressed in terms of the aspect ratio ( $AR$ ) of the wing as  $L = AR \times b$ , where  $b$  is the semichord of the wing. In order to get nondimensionalized equations, the dependent variables  $v, w, \phi$ , and the independent variable  $t$ , are made dimensionless by introducing the characteristic length,  $b$ , and the characteristic time,  $\sqrt{\frac{mb^4}{D_\phi}}$ . The characteristic time adopted in this study is inversely proportional to the system's natural frequency. The dependent variables and system parameters are written in nondimensional form as follows

$$\begin{aligned} v^* &= \frac{v}{b}, & w^* &= \frac{w}{b}, & e^* &= \frac{e}{b}, & t^* &= t \sqrt{\frac{D_\phi}{mb^4}}, & I_\zeta^* &= \frac{I_\zeta}{mb^2}, \\ I_\phi^* &= \frac{I_\phi}{mb^2}, & I_\eta^* &= \frac{I_\eta}{mb^2}, & \beta_\phi &= \frac{D_\phi}{D_\zeta}, & \beta_\eta &= \frac{D_\eta}{D_\zeta}, & \mu^* &= \frac{\pi \rho b^2}{m}, \\ V^* &= \frac{V}{\sqrt{D_\phi/mb^2}}, & AR &= \frac{L}{b} \end{aligned}$$

Now, the nonlinear equations of motion for a cantilever wing can be rewritten in nondimensional form as follows. To simplify the notation in the following analysis, the '\*' superscript is omitted. Letting the prime denote the nondimensional spatial derivative and dot non-dimensional time derivative, the equation of motion can be expressed as

$$\begin{aligned} m\ddot{w} - \frac{I_\eta}{AR^2} \ddot{w}'' + \frac{1}{\beta_\phi} \frac{\beta_\eta}{AR^4} u^{IV} &= G'_w + qbC_A \\ m\ddot{v} - m\ddot{\phi} - \frac{I_\zeta}{AR^2} \ddot{v}'' + \frac{1}{\beta_\phi} \frac{1}{AR^4} w^{IV} &= G'_v + qbC_N \end{aligned}$$

$$I_\phi \ddot{\phi} - m\ddot{v} - \frac{1}{AR^2} \phi'' = G_\phi + qb^2 C_M \quad (2.15)$$

where

$$\begin{aligned} G'_w = & \frac{1}{AR} \left\{ \frac{1}{AR^2} \left( \frac{1}{AR} \phi' + \frac{1}{AR^3} v'' w' \right) v'' - \frac{1}{AR^3} \left[ \left( \frac{\beta_\eta}{\beta_\phi} - \frac{1}{\beta_\phi} \right) (\phi v'' + \phi^2 w'') \right]' \right. \\ & - \frac{1}{AR^5} w' \left( \frac{1}{\beta_\phi} v''^2 + \frac{\beta_\eta}{\beta_\phi} w''^2 \right) - \frac{1}{AR} I_\xi \left( \dot{\phi} + \frac{1}{AR^2} \dot{v}' w' \right) \dot{v}' \\ & - \frac{1}{AR} [(I_\eta - I_\zeta) (\phi \dot{v}' + \phi^2 \dot{w}')]^\bullet + \frac{1}{AR^3} w' (I_\zeta \dot{v}'^2 + I_\eta \dot{w}'^2) \\ & - \frac{1}{AR^5} w' \left( \frac{1}{\beta_\phi} v' v''' + \frac{\beta_\eta}{\beta_\phi} w' w''' \right) + \frac{1}{AR^3} w' (I_\zeta \ddot{v}' v' + I_\eta \ddot{w}' w') \\ & \left. - \frac{1}{AR^2} w' \left[ \int_1^s \left( \frac{1}{2} m \left[ \int_0^s (v'^2 + w'^2) d\hat{x} \right]^{\bullet\bullet} + qb C_u \right) dx \right] + \frac{1}{AR^3} v' w' w' qb^2 C_M \right\}' \end{aligned}$$

$$\begin{aligned} G'_v = & \frac{1}{AR} \left\{ -\frac{1}{AR^2} \left( \frac{1}{AR} \phi' + \frac{1}{AR^3} v'' w' \right) w'' \right. \\ & - \frac{1}{AR} \left[ \left( \frac{\beta_\eta}{\beta_\phi} - \frac{1}{\beta_\phi} \right) \left( \frac{1}{AR^2} \phi^2 v'' - \frac{1}{AR^2} \phi w'' - \frac{1}{AR^4} v' w' w'' \right) \right]' \\ & - \frac{1}{AR^5} v' \left( \frac{1}{\beta_\phi} v''^2 + \frac{\beta_\eta}{\beta_\phi} w''^2 \right) + \frac{1}{AR} I_\xi \left( \dot{\phi} + \frac{1}{AR^2} \dot{v}' w' \right) \dot{w}' \\ & + \left[ (I_\eta - I_\zeta) \left( \frac{1}{AR} \phi^2 \dot{v}' - \frac{1}{AR} \phi \dot{w}' - \frac{1}{AR^3} v' w' \dot{w}' \right) \right]^\bullet + \frac{1}{AR^3} v' (I_\zeta \dot{v}'^2 + I_\eta \dot{w}'^2) \\ & - \frac{1}{AR^5} v' \left( \frac{1}{\beta_\phi} v' v''' + \frac{\beta_\eta}{\beta_\phi} w' w''' \right) + \frac{1}{AR^3} v' (I_\zeta \ddot{v}' v' + I_\eta \ddot{w}' w') \\ & - \frac{1}{AR^2} v' \left[ \int_1^s \left( \frac{1}{2} m \left[ \int_0^s (v'^2 + w'^2) d\hat{x} \right]^{\bullet\bullet} + qb C_u \right) dx \right] \\ & \left. + \frac{1}{AR^3} w' v' v' qb^2 C_M + \frac{1}{AR} w' qb^2 C_M \right\}' \end{aligned}$$

$$\begin{aligned} G_\phi = & \frac{1}{AR^4} (w' v'')' - \frac{1}{AR^4} \left( \frac{\beta_\eta}{\beta_\phi} - \frac{1}{\beta_\phi} \right) [(v''^2 - w''^2) \phi - v'' w''] \\ & - \frac{1}{AR^2} I_\xi (w' \dot{v}')^\bullet + \frac{1}{AR^2} (I_\eta - I_\zeta) [(\dot{v}'^2 - \dot{w}'^2) \phi - \dot{v}' \dot{w}'] \end{aligned}$$

In this form, the effect of AR and  $\beta$  on the equations of motion is evident. A few important observations are made about these equations. First, in-plane motion is included. This assumption is required for high aspect-ratio vehicles. Second, the

right-hand side of the equations contains the nonlinear terms (including the aerodynamic terms). We note that dynamics of interest for the nonlinear system become evident for certain classes of the stiffness ratio  $\beta_\eta$  and aspect ratio,  $AR = \text{span}/\text{chord}$ . These nonlinearities may be classified into 3 sets: (a) geometric stiffening effects due to large structural deformations, (b) damping-induced nonlinearities due to motion; and, (c) aerodynamic nonlinearities as captured in  $N$ ,  $A$  and  $M_{EA}$ . Third, the parameter space is vast, requiring the need for sensitivity and bifurcation analysis.

## B. Solution Procedure

The solution is assumed to be separable in space and time. The variables are expressed in series form as follows:

$$w(x, t) = \sum_{i=1}^{\infty} W_i(x)w_i(t), \quad (2.16)$$

$$v(x, t) = \sum_{j=1}^{\infty} V_j(x)v_j(t), \quad (2.17)$$

$$\phi(x, t) = \sum_{k=1}^{\infty} A_k(x)\phi_k(t) \quad (2.18)$$

where  $w_i(t)$ ,  $v_j(t)$  and  $\phi_k(t)$  represent the generalized (modal) coordinate of the system. In these expressions, the capitalized terms,  $W_i$ ,  $V_j$  and  $A_k$  represent the shape functions derived from a vibrating, nonrotating uniform cantilever beam, and they are defined as follows:

$$\begin{aligned} W_i(x) = F_i(x) &= \cosh\left(\frac{\beta_i x}{L}\right) - \cos\left(\frac{\beta_i x}{L}\right) - \sigma_i \left[ \sinh\left(\frac{\beta_i x}{L}\right) - \sin\left(\frac{\beta_i x}{L}\right) \right] \\ V_j(x) = F_j(x) &= \cosh\left(\frac{\beta_j x}{L}\right) - \cos\left(\frac{\beta_j x}{L}\right) - \sigma_j \left[ \sinh\left(\frac{\beta_j x}{L}\right) - \sin\left(\frac{\beta_j x}{L}\right) \right] \\ A_k(x) &= \sqrt{2} \sin\left(\frac{\gamma_k x}{L}\right) \end{aligned} \quad (2.19)$$

The  $F_i(s)$ ,  $F_j(s)$  and  $A_k(s)$  are mode shapes or shape functions for in-plane, out-of-plane bending and torsion motion respectively. Here,  $\beta_i$  is a root of the characteristic equation for pure bending,

$$1 + \cos(\beta) \cosh(\beta) = 0 \quad (2.20)$$

and  $\sigma_i$  is defined as

$$\sigma_i = \frac{\cosh(\beta_i) + \cos(\beta_i)}{\sinh(\beta_i) + \sin(\beta_i)} \quad (2.21)$$

and  $\gamma_k$  is a root of the characteristic equation for pure torsion motion  $\sin(2\gamma_k) = 0$ .

By using the Galerkin method, the corresponding ordinary differential equations (ODEs) can be obtained from the above partial differential equations (PDEs). The procedure is applied to obtain linear mass, damping and stiffness matrices. These matrices are time invariant. Thus, they are computed only once.

Let  $l$ ,  $m$  and  $n$  be number of in-plane, out-of-plane and torsion modes respectively used in the solution. The elements of the linear mass matrix are computed as follows

$$\begin{aligned} M_{i,j} &= \int_0^L W_i(x) \left( mW_j(x) - I_\eta W_j''(x) \right) dx \quad 1 \leq i \leq l, \quad 1 \leq j \leq l \\ M_{l+i,l+j} &= \int_0^L V_i(x) \left( mV_j(x) - I_\zeta V_j''(x) \right) dx \quad 1 \leq i \leq m, \quad 1 \leq j \leq m, \\ M_{l+i,l+m+j} &= -me \int_0^L V_i(x) A_j(x) dx \quad 1 \leq i \leq m, \quad 1 \leq j \leq n \\ M_{l+m+i,l+j} &= -me \int_0^L A_i(x) V_j(x) dx \quad 1 \leq i \leq n, \quad 1 \leq j \leq m \\ M_{l+m+i,l+m+j} &= I_\xi \int_0^L A_i(x) A_j(x) dx \quad 1 \leq i \leq n, \quad 1 \leq j \leq n \end{aligned} \quad (2.22)$$

The subscript denote the row and column position within the matrix. The elements of mass matrix not listed in Eq. 2.22 are zero. The elements of the linear stiffness matrix are computed as follows:

$$K_{i,j} = D_\eta \int_0^L W_i(x) W_j''''(x) dx \quad 1 \leq i \leq l, \quad 1 \leq j \leq l$$

$$\begin{aligned}
K_{l+i,l+j} &= D_\zeta \int_0^L V_i(x) V_j''''(x) dx \quad 1 \leq i \leq m, \quad 1 \leq j \leq m \\
K_{l+m+i,l+m+j} &= -D_\xi \int_0^L A_i(x) A_j''(x) dx \quad 1 \leq i \leq n, \quad 1 \leq j \leq n
\end{aligned} \tag{2.23}$$

Again, the elements of stiffness matrix not listed in Eq. 2.23 are zero. The linear damping matrix is zero.

These matrices can be used to determine the natural frequencies and damping for the structural system. These frequencies and damping are however modified by deformation and rate dependent aerodynamic loads. The nonlinear components of the PDEs are separated into inertia and non-inertia type of term. Any term which involves double time derivative is inertia term. For example, a nonlinear inertia term in the out-of-plane bending equation is  $\{v' I_\zeta \ddot{v}' v'\}'$ .

The nonlinear inertia terms are expressed as the nonlinear mass matrix  $[M_{NL}]$  multiplied by the vector of accelerations. However, unlike the linear case the nonlinear mass matrix,  $[M_{NL}]$ , is a function of states and thus time dependent. Therefore,  $[M_{NL}]$  is computed at every time step. The nonlinear stiffness and damping terms are expressed as nonlinear forcing vector  $F_{NL}$ . After separating the nonlinear inertia terms, the presence of a prime in all of the terms is exploited to simplify the integration procedure. To illustrate the procedure, the nonlinear component for the  $i^{th}$  in-plane bending equations is obtained as follows by application of Galerkin method

$$G_w^i = \int_0^L W_i(x) G_w'(x, t) dx$$

Note, that the  $G_w'$  in the above equation does not contain the nonlinear inertia terms shown in Eq. (2.13). Integrating this equation by parts

$$G_w^i = \left[ (W_i(L) G_w(L, t) - W_i(0) G_w(0, t)) - \int_0^L W_i'(x) G_w(x, t) dx \right] \tag{2.24}$$



This approach simplifies the expansion of the nonlinear terms. All nonlinear components are obtained in similar manner. However,  $G_\phi$  does not possess spatial derivative; hence, there is no need follow this approach to obtain the nonlinear stiffness and damping components of the torsion equation. The ODEs obtained are expressed in matrix form as:

$$[M_L] \begin{Bmatrix} \ddot{w} \\ \ddot{v} \\ \ddot{\phi} \end{Bmatrix} + [C_L] \begin{Bmatrix} \dot{w} \\ \dot{v} \\ \dot{\phi} \end{Bmatrix} + [K_L] \begin{Bmatrix} w \\ v \\ \phi \end{Bmatrix} = [M_{NL}] \begin{Bmatrix} \ddot{w} \\ \ddot{v} \\ \ddot{\phi} \end{Bmatrix} + F_{NL} + F_A \quad (2.25)$$

where  $F_{NL}$  is the vector of the structural nonlinear terms excluding the inertia terms.  $F_A$  is the vector of aerodynamic forces and moments obtained after the application of the Galerkin procedure to the physical loads. This procedure interpolates the aerodynamic loads between the modal degrees of freedom. Equation (2.25) is rearranged as follows

$$\begin{Bmatrix} \ddot{w} \\ \ddot{v} \\ \ddot{\phi} \end{Bmatrix} = ([M_L] - [M_{NL}])^{-1} \times \left( -[C_L] \begin{Bmatrix} \dot{w} \\ \dot{v} \\ \dot{\phi} \end{Bmatrix} - [K_L] \begin{Bmatrix} w \\ v \\ \phi \end{Bmatrix} + F_{NL} + F_A \right) \quad (2.26)$$

The vectors  $w$ ,  $v$  and  $\phi$  in Eq. (2.25) and Eq. (2.26) represent in-plane, out-of-plane and torsion modal coordinates, and given as follows

$$w = \begin{Bmatrix} w_1 \\ w_2 \\ \cdot \\ \cdot \\ w_l \end{Bmatrix}, \quad v = \begin{Bmatrix} v_1 \\ v_2 \\ \cdot \\ \cdot \\ v_m \end{Bmatrix}, \quad \phi = \begin{Bmatrix} \phi_1 \\ \phi_2 \\ \cdot \\ \cdot \\ \phi_n \end{Bmatrix} \quad (2.27)$$

The indices  $l$ ,  $m$  and  $n$  in Eq. (2.27) are the number of in-plane, out-of-plane and torsion modes, respectively, used in the solution. Defining the state vector as follows

$$X = \{w_1, w_2, \dots, w_l, v_1, v_2, \dots, v_m, \phi_1, \phi_2, \dots, \phi_n, \dot{w}_1, \dot{w}_2, \dots, \dot{w}_l, \dot{v}_1, \dot{v}_2, \dots, \dot{v}_m, \dot{\phi}_1, \dot{\phi}_2, \dots, \dot{\phi}_n\} \quad (2.28)$$

the equations of motion are represented in state-space form as

$$\{\dot{X}\} = \left\{ \begin{array}{c} \dot{w} \\ \dot{v} \\ \dot{\phi} \\ ([M_L] - [M_{NL}])^{-1} \times \left( -[C_L] \begin{Bmatrix} \dot{w} \\ \dot{v} \\ \dot{\phi} \end{Bmatrix} - [K_L] \begin{Bmatrix} w \\ v \\ \phi \end{Bmatrix} + F_{NL} + F_A \right) \end{array} \right\} \quad (2.29)$$

A Runge-Kutta algorithm [9] is used for time integration of Eq. (2.29). It is now easy to see the need for explicit separation of nonlinear inertia terms and construction of nonlinear mass matrix  $[M_{NL}]$ . This separation allows the equations to be expressed in state-space required by the Runge-Kutta algorithm.

### C. Validation of Code

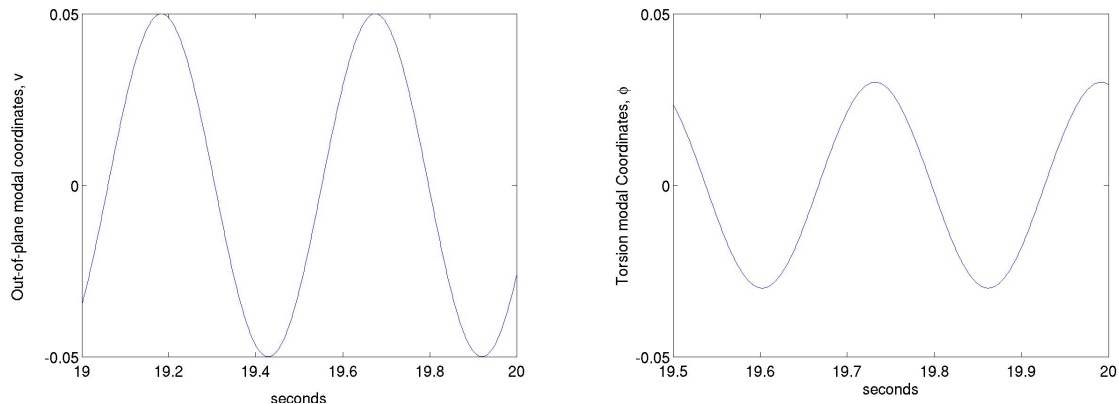
Figure 4 shows linear structural dynamic response for heavy Goland wing. Only one mode for each degree of freedom was used. The time period for out-of-plane bending oscillation of the first mode is given by:

$$T_v^1 = 2\pi \left( \frac{L}{\beta_1} \right)^2 \sqrt{\frac{m}{D_\zeta}} = 0.5027 \quad (2.30)$$

The time period for first torsion mode is given by:

$$T_\phi^1 = 2\pi \left( \frac{L}{\pi/2} \right) \sqrt{\frac{I_\xi}{D_\xi}} = 4L \sqrt{\frac{I_\xi}{D_\xi}} = 0.2596 \quad (2.31)$$

As seen in Fig. 4, the time period for steady state oscillation matches with theoretical time period given by Eq. 2.30 and Eq. 2.31. Figure 5 compares the result produced



(a) Out-of-plane steady state response

(b) Torsion steady state response

Fig. 4. Verification of code: Out-of-plane and torsion free response of heavy Golland wing illustrating matching time period of motion

for a test case with the current code with that given in [5]. The simulation plot is for heavy Golland wing [5] with linear structure and aerodynamics. The result is in agreement with that given in Ref. [5]. Figure 6 provides further verification. It shows the system response at 210 ft/sec which 30 ft/sec excess of flutter velocity. The left view shows transient response immediately following initial displacement. The right view shows steady state oscillations. The transient response and steady state amplitudes compare extremely well with Ref. [5]. All the above results verify that the algorithm has been properly implemented.

#### D. Evaluation of System Dynamics

For the purposes of addressing term sensitivity in the structural equations, a quasi-steady approach is used to compute the aerodynamic loads. The authors use the software tool, AUTO[10], for continuation and bifurcation analyses of the nonlinear ordinary differential equations. AUTO automates the computation of solutions of this

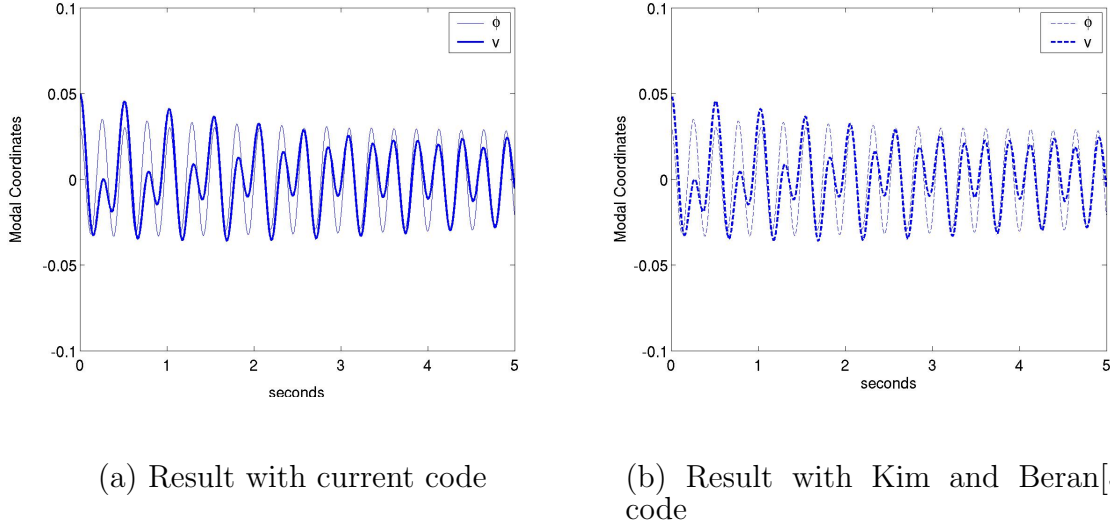


Fig. 5. Validation of code:  $V=100$  ft/sec, heavy Goland wing with linear structure and linear aerodynamics; initial condition:  $(v, \phi, \dot{v}, \dot{\phi}) = (0.05, 0.03, 0, 0)$

parameter-dependent system of equations. The system possesses multiple solutions, and it is valuable to compute the set of solutions and search for those solutions with specific desirable properties as a system parameter is varied. This solution set forms a bifurcation diagram, i.e., a smooth curve (or surface) representing the solution for the varying system parameter. Tools such as AUTO2000 facilitate parametric studies and minimize time consuming numerical simulations. The computation of such bifurcation diagrams and associated singularities is captured within the domain of the numerical continuation algorithm [11, 12]. AUTO has the capability to compute periodic solutions such as the limit cycle oscillations discussed in this paper. In addition, the program determines the stability of the steady state solutions. AUTO permits a two-parameter continuation solution of Hopf and other bifurcation points. A detailed description on the features of software can be found in the AUTO Manual[13].

The equations of motion must be presented in state space form and a known solution must be provided as an initial point. Continuation solutions are conducted

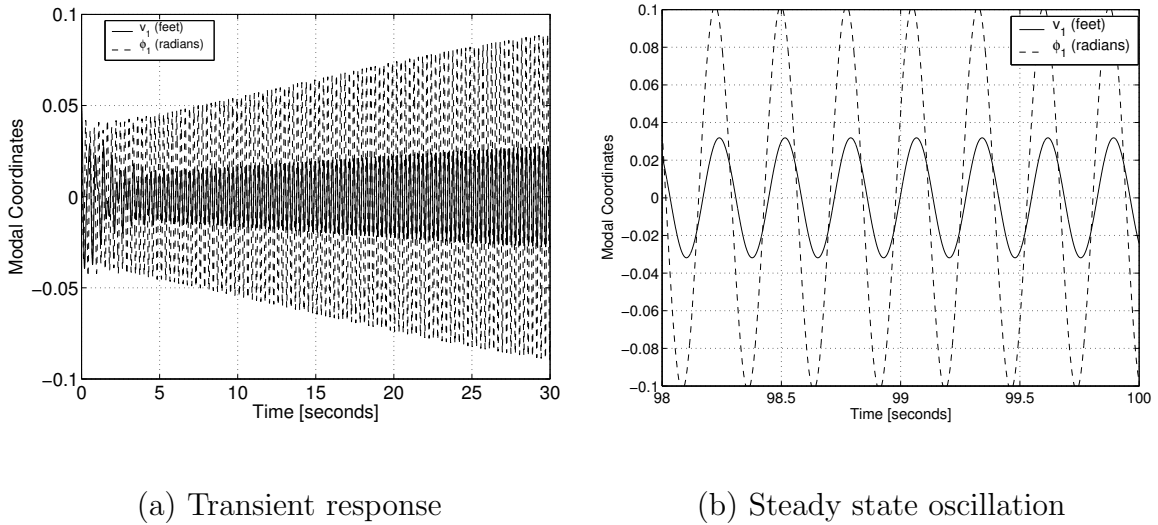


Fig. 6. Time response of heavy Goland wing at  $V=210$  ft/sec; initial condition:  $(v, \phi, \dot{v}, \dot{\phi}) = (0.05, 0.03, 0, 0)$

starting at this known solution, and all of the equilibrium points are computed automatically as a system parameter is varied. In this process, the critical value of parameters of interest at which bifurcation occurs is also computed. For our computations, the freestream velocity is varied. The flutter point is detected as a Hopf bifurcation.

Term by term analysis of the nonlinear terms in the Eqs. (2.15) reveal that the dynamics of the system are governed by the parameter  $\beta_\eta$ , which is defined as the ratio of stiffness between the in-plane and out-of-plane bending modes. We are interested in the effect of  $\beta_\eta$  as the system exhibits dramatically different dynamics. Thus, results from two representative values of  $\beta_\eta$  are compared.

For high values of (e.g.,  $\beta_\eta > 10$ ), the coupling between in-plane and out-of-plane bending response is not significant and the nonlinear stiffness terms dominate the system dynamics. Such a case is representative of conventional aircraft configurations. Most of the nonlinear inertia and damping terms have little or no influence on

Table I. Baseline values of the parameters for NATA wing

Parameter	Value
Semichord, $b$	0.1350 $m$ (0.443 $ft$ )
Wing semispan, $L$	1.200 $m$ (3.94 $ft$ )
mass density, $m$	1.973 $kg/m$ (0.041 $slug/ft$ )
Out-of-plane bending stiffness, $D_\zeta$	476.9 $Nm^2$ (1154.72 $lb\ ft^2$ )
In-plane bending stiffness, $D_\eta$	20980 $Nm^2$ (50799 $lb\ ft^2$ )
Torsional stiffness, $D_\xi$	3.988 $Nm^2$ (9.656 $lb\ ft^2$ )
Pitch inertia, $I_\xi$	0.0527 $kg\ m$ (0.0116 $slug\ ft$ )

the bifurcation characteristics of the system. However, this behavior is significantly different for low values of  $\beta_\eta$ . At low values of (e.g.,  $\beta_\eta < 10$ ), most nonlinear terms influence the system dynamics.

The influence of each term on the bifurcation characteristics of the system is investigated by comparing the bifurcation characteristics of the original system with the characteristics of the system with specific nonlinear terms removed. Alternatively, each nonlinear term is added one by one and its influence on the bifurcation characteristics is studied. The baseline values of system parameters are provided in Table I. The parameters are based upon a modified version of the physical properties of the Nonlinear Aeroelastic Test Apparatus (NATA). For this case,  $\beta_\eta = 44.0$ .

The  $(\beta_\eta - 1)v''^2\phi$  term in the torsion equation is the primary source for sub-critical bifurcation behavior. This behavior is illustrated in Fig. 5 which compares the bifurcation characteristics of the full nonlinear system with the system that has the term  $(\beta_\eta - 1)v''^2\phi$  removed. In these diagrams, stable branches (limit cycles, attractors, equilibria, etc) are shown with solid lines; unstable branches are shown by

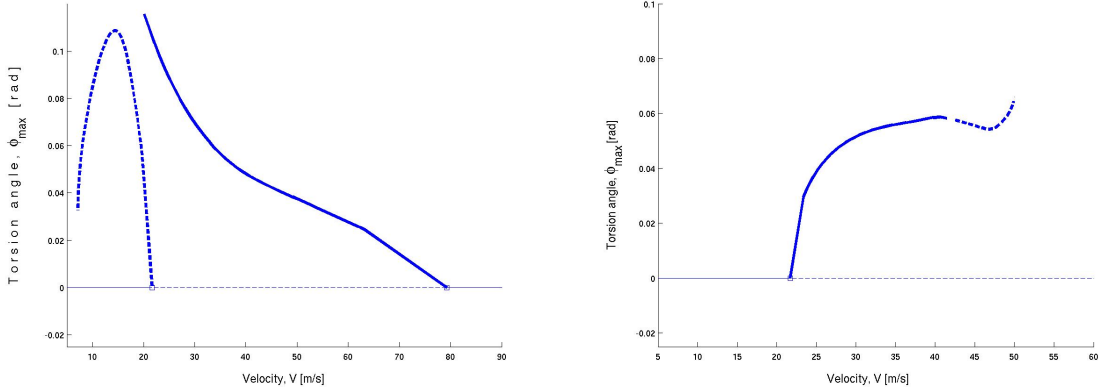


Fig. 7. Comparison of bifurcation diagrams with  $(\beta_\eta - 1)v''^2\phi$  retained(left view) and removed(right view)

dashed lines; and, bifurcation points are shown by the symbol (square). If the term is removed, a supercritical stable LCO branch, instead of a subcritical unstable LCO branch, emanates from the Hopf bifurcation point. Thus, the subcritical bifurcation exhibited by certain aircraft wing configurations is caused by the cubic stiffness term coupling out-of-plane bending and torsion motion.

The quadratic coupling terms between in-plane and other wing bending modes significantly affect the amplitude of LCO. Figure 6 shows the bifurcation diagram with terms represented by the quadratic terms removed. A substantial reduction in LCO amplitude is observed. It is noted that most of the nonlinear wing inertia terms are small compared to the nonlinear stiffness terms. Likewise, the nonlinear damping terms are small compared to the nonlinear stiffness terms. The bifurcation characteristics shown in Fig. 5 are unaffected when these nonlinear terms are removed. Consequently, the nonlinear equations may be simplified for certain cases, but the response depends upon  $\beta_\eta$  and  $AR$ .

The system dynamics are examined at lower values of  $\beta_\eta$ . In the following analysis  $\beta_\eta = 2$ ; all other parameters are as stated in Table 1. For this lower value of  $\beta_\eta$ , the

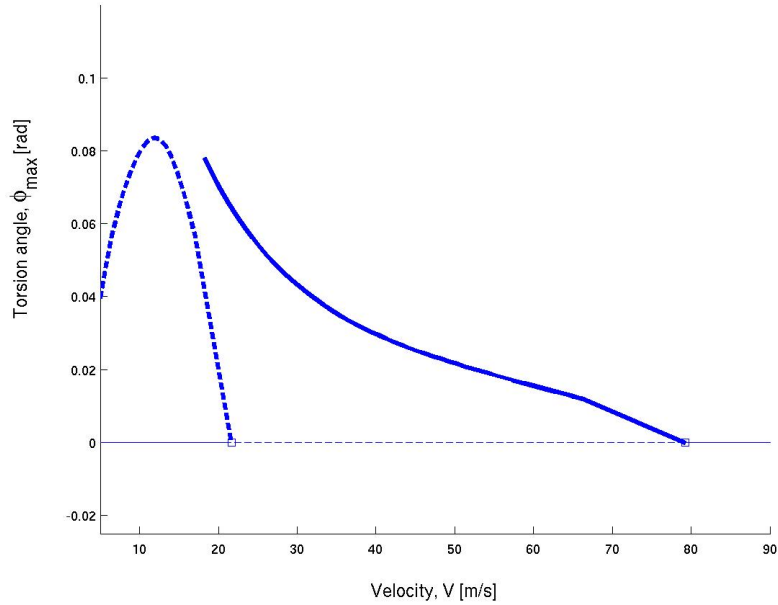


Fig. 8. Bifurcation diagram with term  $(\beta_\eta - 1)(v''\phi)''$  and  $(\beta_\eta - 1)(v''w'')$  removed

in-plane and out-of-plane stiffnesses are similar; consequently, the system exhibits significantly different dynamics than the previous case. The nonlinear inertia and damping terms which had no influence at higher  $\beta_\eta$  now contribute to the response. For the two stiffness ratio cases,  $\beta_\eta = 2$  and 44, the bifurcation characteristics of the system with all nonlinear terms retained are compared in Fig. 7.

Figure 8 shows the bifurcation characteristics for  $\beta_\eta = 2$  with the integral term removed. The amplitudes of both stable and unstable limit cycles are different from that seen in Fig. 7. Unlike the previous case, the cubic integral terms greatly affect the dynamics of the system.



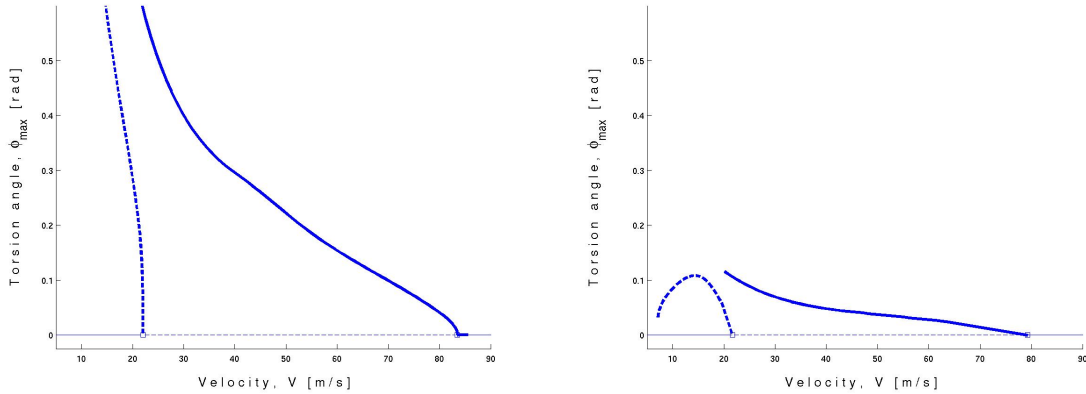


Fig. 9. Bifurcation diagram for system with  $\beta_\eta = 2$  (left view) and  $\beta_\eta = 44$  (right view); all nonlinear terms retained

### E. Internal Resonance

This section discusses possible large amplitude in-plane motion via an internal resonance mechanism. Internal resonance occurs as a result of nonlinearities present in the system. It leads to exchange of energy between system modes [14]. Internal resonance exists when the linear natural frequencies of system are commensurable, or nearly so, and the nonlinearities of the system provide a source of coupling. External forcing is available from the flowfield. Commensurability is defined by  $m_1\omega_1 + m_2\omega_2 + \dots + m_n\omega_n \approx 0$ , where  $m_n$  can be a positive or negative integer and  $\omega_n$  are the natural frequencies of the system. Although an integer natural frequency ratio does not guarantee internal resonance, it does form a necessary condition[15]. Nayfeh and Balachandran [16] describe that a 2:1 internal resonance may occur when quadratic nonlinearities are present, and 3:1 internal resonance may occur when cubic nonlinearities are present.

As a test case, the heavy Golland wing (HGW) is used with parameters shown in Table II. The aspect ratio ( $AR$ ) of the HGW is 6.67. Figure 10 shows the bifurcation diagram for the HGW with the wing length,  $L$ , as the free parameter. The velocity is

Table II. Baseline values of the parameters for the heavy Goland wing[17]

Parameter	Value
Semichord, $b$	0.914 $m$ (3 $ft$ )
Wing semispan, $L$	6.096 $m$ (20 $ft$ )
mass per unit span, $m$	538.57 $kg/m$ (11.249 $slug/ft$ )
Out-of-plane bending stiffness, $D_\zeta$	$9.772 \times 10^6 \text{ Nm}^2$ ( $23.647 \times 10^6 \text{ lb ft}^2$ )
In-plane bending stiffness, $D_\eta$	$9.772 \times 10^8 \text{ Nm}^2$ ( $23.647 \times 10^6 \text{ lb ft}^2$ )
Torsional stiffness, $D_\xi$	$9.871 \times 10^5 \text{ Nm}^2$ ( $2.3899 \times 10^6 \text{ lb ft}^2$ )
Pitch inertia, $I_\xi$	111.955 $kg m$ (25.17 $slug ft$ )
Elastic axis,	0.6096 $m$ (2 $ft$ ) from LE
Centroidal axis	0.792 $m$ (2.6 $ft$ ) from LE

maintained at 140 ft/sec and the wing length is varied between 10 feet and 100 feet ( $AR > 30$ ). The torsion angle equilibria and periodic solutions are indicated. Three Hopf bifurcations are encountered. Stable limit cycle oscillation (LCO) response occurs for approximately  $10 < L < 20$  ft. The wing is stable without LCO for  $20 < L < 40$  ft. Then, stable LCO response occurs for  $L > 40$  ft.

Figure 11 shows the in-plane bending periodic solutions for various wing lengths for a velocity of 108 ft/sec. A sharp increase in the in-plane response amplitude is observed beyond the third Hopf bifurcation associated with a critical wing length. Numerical simulations at this critical length are shown in Fig. 12 which clearly illustrates the exchange in energy between the in-plane and out-of-plane modes. The in-plane amplitude is greater than the out-of-plane amplitude. Furthermore, at this velocity, there is a 2:1 frequency ratio between in-plane and torsion responses. This behavior is attributed to internal resonance between in-plane and torsion motion.

The locus of the third Hopf bifurcation in Velocity-Length ( $V$ - $L$ ) parameter space can be obtained by a two-parameter numerical continuation method [13]. Such a locus is illustrated in Fig. 13. The system will exhibit LCO in the region above the curve and would have stable dynamics in the region below the curve. The critical region where the system can exhibit internal resonance has been boxed. The wing length at which the resonance phenomenon occurs is dependent on freestream velocity. Moreover, the freestream velocity need to be above a threshold value. Thus, for values below this threshold value no internal resonance is seen. This value is found to be  $V=108$  ft/sec for the system under consideration.

Figure 14 shows bifurcation diagram with  $L$  as the parameter at free-stream velocity of 107 ft/sec. Unlike the previous case no resonance is seen. The Velocity-Length resonance pair has been plotted in Fig. 15. With increasing velocity, the critical length value decreases first and then gradually increases.

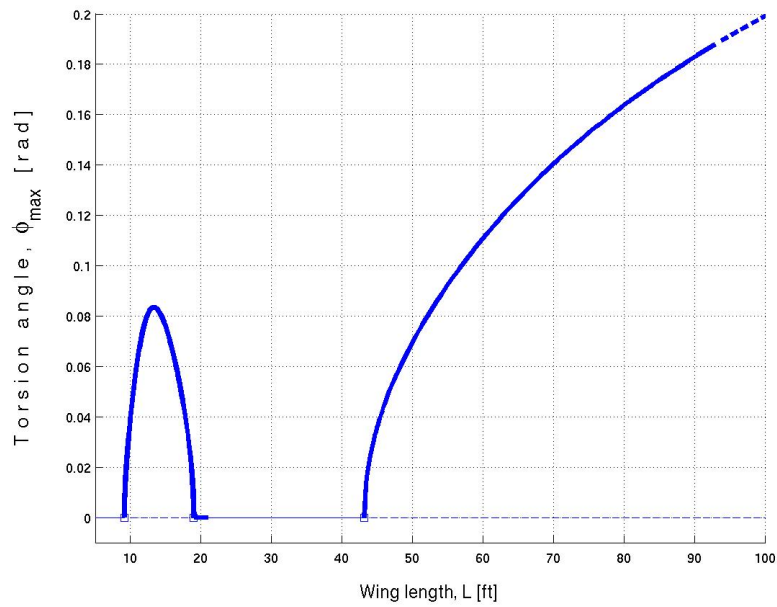


Fig. 10. Bifurcation diagram with  $L$  as parameter

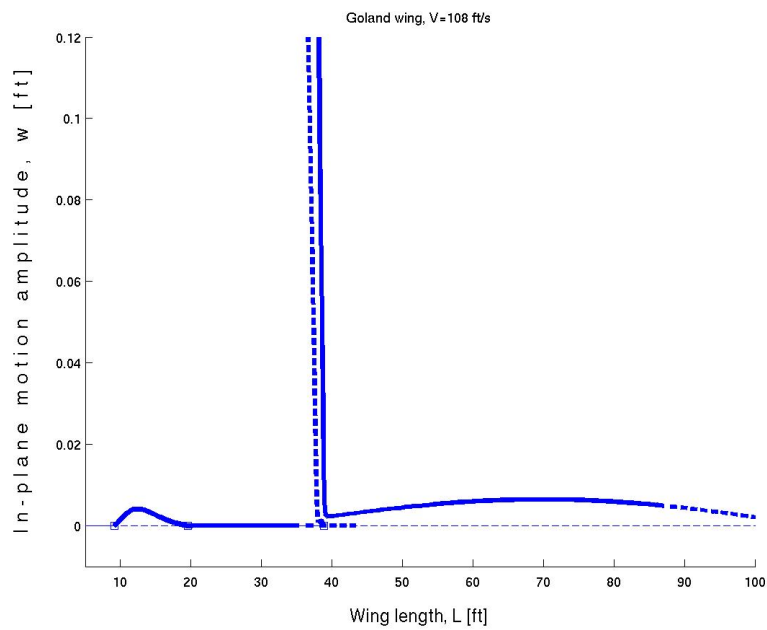


Fig. 11. Bifurcation diagram at  $V = 108$  ft/sec illustrating internal resonance

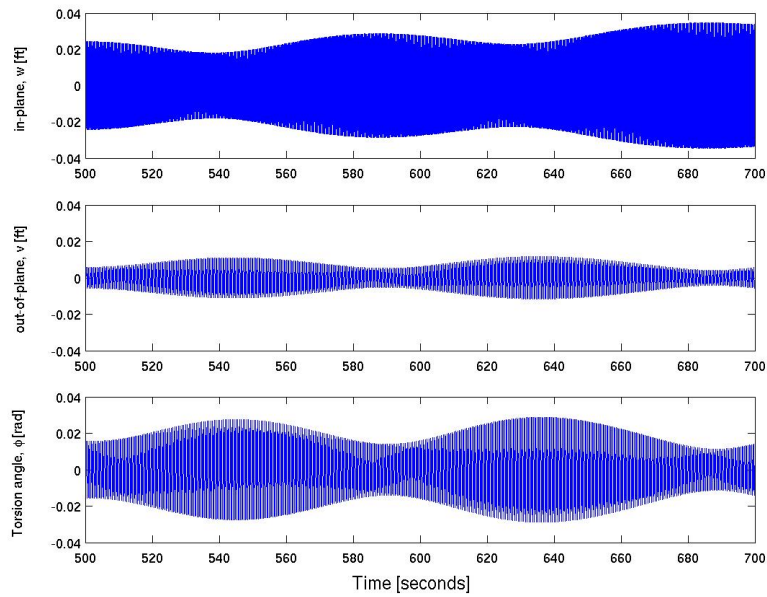


Fig. 12. Simulation illustrating internal resonance (heavy Goland wing,  $V = 108$  ft/sec,  $L = 38$  ft and  $\beta_\eta = 44$ )

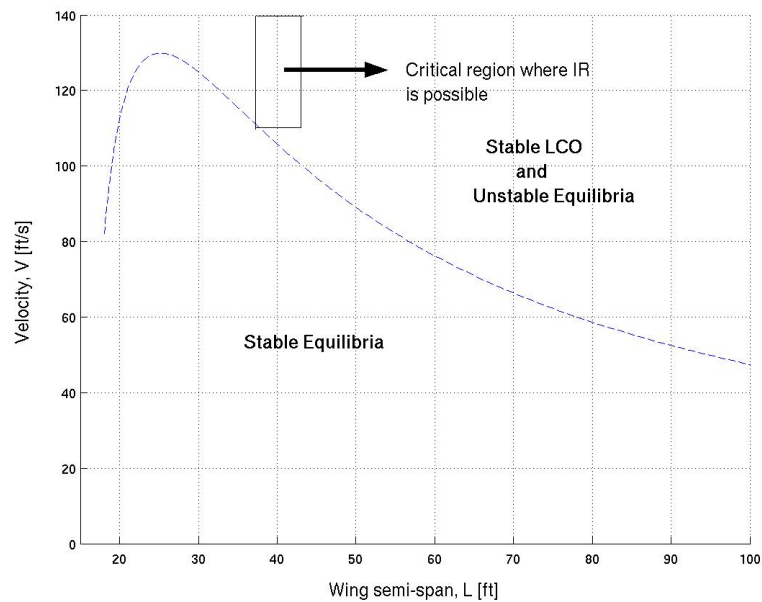


Fig. 13. Locus of Hopf bifurcation in  $V$ - $L$  parameter space

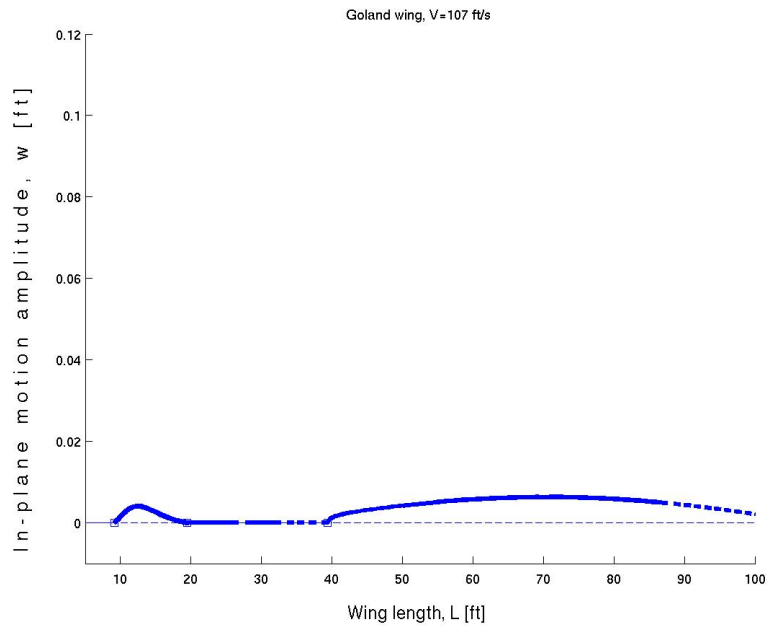


Fig. 14. Bifurcation diagram at  $V = 107$  ft/sec showing absence of resonance

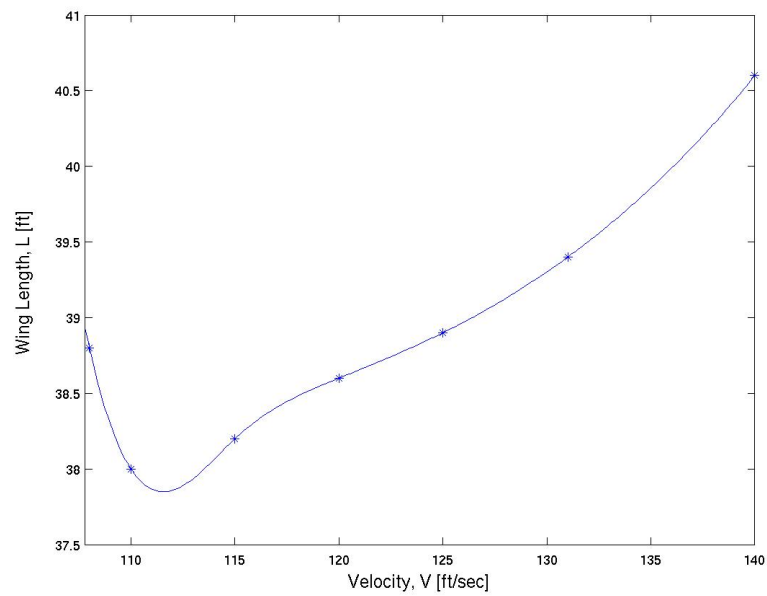


Fig. 15. Velocity-Length internal resonance pair

## CHAPTER III

FORMULATION II: THREE DIMENSIONAL MOTION ABOUT NONZERO  
EQUILIBRIA

A limiting feature of all of the studies in the previous chapter is the Taylor series expansion of structural nonlinearities about a particular equilibria which was zero undeformed equilibria. The structural nonlinearities occur as the second and higher order terms in a series expansion. Nonlinear terms of order four and higher have been neglected in all of the above work. This approach assumes that terms become negligible as one moves to higher order. Thus, there is an implicit assumption here that the values of the nonlinear terms are much less than the linear terms. It is also assumed that the nonlinear terms would have diminishing values with increasing exponent. However, for very large deformations the vice-versa holds true. Thus, analysis with all of the above formulations must be limited to "moderately" large deformation about zero equilibria. The use of the term word "moderate" is qualitative here. The domain of deformation for which the analysis would be valid depends on the magnitude of the nonlinear terms which must have diminishing value with increasing exponent to justify the neglect of higher order terms. Most importantly, the Taylor series expansion is always performed about a point and the nonlinear expression would be different if the same series expansion is performed about a non-zero equilibria. The trim shape of the wing calculated using these equations would be erroneous because the formulation to begin with assumes zero trim. Thus, a set of exact full nonlinear expressions without resorting to polynomial Taylor expansion needs to be used in the analysis.

The configuration space and flight regimes of such vehicles is vast involving numerous design parameters such as aspect ratio, structural stiffness, weight etc. De-

termination of nonlinear trim states and their stability is thus a challenge that must be addressed in an efficient manner. Also, the structural vibration mode can significantly couple with rigid body vehicle modes. Patil and Hodges[18] have reported that the structural mode under certain conditions can destabilize the Phugoid mode of aircraft longitudinal dynamics. They used an intrinsic formulation for the beam where the primary variables are forces and moments on the vehicle. The displacements and rotations are obtained through intrinsic kinematic equations. The formulation has a relatively simpler form compared to that presented here, but the displacement and rotations must be obtained by using additional kinematic relations which complicates the formulation. Mathematically, both formulations are equivalent and geometrically exact. However, the method that is presented in this paper also renders the capability to predict and characterize LCOs in addition to vehicle trim states. The traditional flutter point may be significantly altered due to large wing deformations and changes in angle of attack[19]. Thus, there is a need to examine the vast design space for static and dynamic stability characteristics of the system.

Numerical continuation methods offer a robust and efficient solution to the above mentioned need. The method permits direct eigenanalysis of the system without resorting to explicit linearization. Thus, the nonlinear trim states and their stability can be evaluated in a continuous manner as a system parameter is varied using the exact nonlinear expressions. Also, the method can be used to examine the presence of LCOs. In such a situation, the dynamic characteristic of the system is dependent on initial condition[20]. This continuation and bifurcation analysis must be supplemented by time domain simulations for which an additional tool must be developed.

Thus, in this chapter nonzero trim states of a flexible wing is examined using the method of numerical continuation. A nonlinear formulation for a cantilevered beam is used to model three dimensional motion of a wing. The kinematic nonlinearities



due to curvature and inertia are retained in their exact form. The nonzero trims and their stability are determined as a system parameter is varied. Various bifurcation points of the system are determined. Limit-cycle oscillations are also investigated for and are characterised in terms of amplitude of vibration. This chapter in particular examines the impact of in-plane degree of freedom on the stability of nonzero trim states. The effect of variation of system parameters such as stiffness ratio, aspect ratio and root angle of attack is also studied.

### A. Physical Model

A beam segment of length  $s$  is shown in Fig. 3. The axes  $(x, y, z)$  are assumed to be fixed in the inertial frame, while  $(\xi, \eta, \zeta)$  are taken to be the principal axes of the beam cross-section at position  $s$ . This axes system is arbitrarily oriented in space with respect to the inertial axes system. The orientation of the  $(\xi, \eta, \zeta)$  system with respect to the  $(x, y, z)$  frame is described by the set of 3-2-1 Euler angles  $\psi(s, t)$ ,  $\theta(s, t)$  and  $\phi(s, t)$ . By letting a prime denote partial differentiation with respect to space and the over dot denote partial differentiation with respect to time, the angular velocity of the  $(\xi, \eta, \zeta)$  system with respect to  $(x, y, z)$  system can be written as:

$$\begin{aligned}\omega(s, t) &= (\dot{\phi} - \dot{\psi} \sin \theta) \hat{\xi} + (\dot{\psi} \cos \theta \sin \phi + \dot{\theta} \cos \phi) \hat{\eta} + (\dot{\psi} \cos \theta \cos \phi - \dot{\theta} \sin \phi) \hat{\zeta} \\ &= \omega_{\xi} \hat{\xi} + \omega_{\eta} \hat{\eta} + \omega_{\zeta} \hat{\zeta}\end{aligned}\tag{3.1}$$

Love's kinetic analogy [21] is used to give a relationship between bending curvature and Euler angles. Simply, dots in the equation are replaced by primes:

$$\begin{aligned}C(s, t) &= (\phi' - \psi' \sin \theta) \hat{\xi} + (\psi' \cos \theta \sin \phi + \theta' \cos \phi) \hat{\eta} + (\psi' \cos \theta \cos \phi - \theta' \sin \phi) \hat{\zeta} \\ &= C_{\xi} \hat{\xi} + C_{\eta} \hat{\eta} + C_{\zeta} \hat{\zeta}\end{aligned}\tag{3.2}$$

The Euler angles are related to displacement variables  $u$ ,  $v$  and  $w$  as shown in Fig. 3 by the following relations:

$$\psi = \tan^{-1} \left( \frac{v'}{1+u'} \right) \quad (3.3)$$

$$\theta = \tan^{-1} \left( \frac{-w'}{\sqrt{(1+u')^2 + v'^2}} \right) \quad (3.4)$$

The third Euler angle  $\phi$  is an independent degree of freedom. The beam is assumed to be inextensional lengthwise. This constraint can be expressed mathematically by the following relation:

$$(1+u')^2 + v'^2 + w'^2 = 1 \quad (3.5)$$

The kinetic energy of the system is given by

$$T = \frac{1}{2}m(\dot{u}^2 + \dot{v}^2 + \dot{w}^2) + \frac{1}{2}(I_\xi\omega_\xi^2 + I_\eta\omega_\eta^2 + I_\zeta\omega_\zeta^2) \quad (3.6)$$

where

$$m(x) = \int \int_A \rho(\eta, \zeta, x) dA$$

is the mass per unit length of the beam and

$$I_\eta(x) = \int \int_A \zeta^2 \rho(\eta, \zeta, x) dA$$

$$I_\zeta(x) = \int \int_A \eta^2 \rho(\eta, \zeta, x) dA$$

$$I_\xi = I_\eta + I_\zeta$$

are specific mass moment of inertias. The quantity  $\rho(\eta, \zeta, x)$  is the material density and  $A$  is the area of the cross section. The strain energy is given by

$$U = \frac{1}{2} \left( D_\xi C_\xi^2 + D_\eta C_\eta^2 + D_\zeta C_\zeta^2 \right) \quad (3.7)$$

$D_\xi(x)$  and  $D_\eta(x)$  are bending stiffnesses while  $D_\zeta(x)$  is the torsional stiffness. In general, these quantities are functions of  $x$ .

The beam may be subjected to distributed loads applied along the span. Let the virtual work of these loads be written as

$$\delta W = Q_u \delta u + Q_v \delta v + Q_w \delta w + Q_\phi \delta \phi$$

where  $Q_u$ ,  $Q_v$ ,  $Q_w$  and  $Q_\phi$  denote the generalized forces associated with virtual displacements  $\delta u$ ,  $\delta v$ ,  $\delta w$  and  $\delta \phi$  respectively. The extended Hamilton's principle [22] is used to derive the governing equations of motion. The principle requires:

$$\begin{aligned} \delta I = \delta \int_{t_1}^{t_2} \int_0^L \left\{ (T - U) + \frac{\lambda}{2} [1 - (1 + u')^2 - v'^2 - w'^2] \right\} \\ + \int_{t_1}^{t_2} \int_0^L (Q_u \delta u + Q_v \delta v + Q_w \delta w + Q_\phi \delta \phi) = 0 \end{aligned} \quad (3.8)$$

By taking the variations in Eq. (3.8) and integrating by parts, the following differential equations of motion are obtained

$$m\ddot{u} - Q_u = \left[ A_\psi \frac{\partial \psi}{\partial u'} + A_\theta \frac{\partial \theta}{\partial u'} + \lambda(1 + u') \right]' = G'_u \quad (3.9)$$

$$m\ddot{v} - Q_v = \left[ A_\psi \frac{\partial \psi}{\partial v'} + A_\theta \frac{\partial \theta}{\partial v'} + \lambda v' \right]' = G'_v \quad (3.10)$$

$$m\ddot{w} - Q_w = \left[ A_\psi \frac{\partial \psi}{\partial w'} + A_\theta \frac{\partial \theta}{\partial w'} + \lambda w' \right]' = G'_w \quad (3.11)$$

$$A_\phi = Q_\phi \quad (3.12)$$

In the above equations,  $A_\psi$ ,  $A_\theta$  and  $A_\phi$  are defined as follows

$$\begin{aligned} A_\psi &= \left[ \frac{\partial(T - U)}{\partial \psi'} \right]' + \left[ \frac{\partial(T - U)}{\partial \dot{\psi}} \right]' - \frac{\partial(T - U)}{\partial \psi} \\ &= \{ D_\xi C_\xi \sin \theta - (D_\eta C_\eta \sin \phi + D_\zeta C_\zeta \cos \phi) \cos \theta \}' \end{aligned}$$

$$+ [(I_\eta \omega_\eta \sin \phi + I_\zeta \omega_\zeta \cos \phi) \cos \theta - I_\xi \omega_\xi \sin \theta]^\bullet \quad (3.13)$$

$$\begin{aligned} A_\theta &= \left[ \frac{\partial(T-U)}{\partial \theta'} \right]' + \left[ \frac{\partial(T-U)}{\partial \dot{\theta}} \right]^\bullet - \frac{\partial(T-U)}{\partial \theta} \\ &= (D_\zeta C_\zeta \sin \phi - D_\eta C_\eta \cos \phi)' - (D_\eta C_\eta \sin \phi + D_\zeta C_\zeta \cos \phi) \psi' \sin \theta \\ &\quad - D_\xi C_\xi \psi' \cos \theta - (I_\zeta \omega_\zeta \sin \phi - I_\eta \omega_\eta \cos \phi)^\bullet \\ &\quad + (I_\eta \omega_\eta \sin \phi + I_\zeta \omega_\zeta \cos \phi) \dot{\psi} \sin \theta + I_\xi \omega_\xi \dot{\psi} \cos \theta \end{aligned} \quad (3.14)$$

$$\begin{aligned} A_\phi &= \left[ \frac{\partial(T-U)}{\partial \phi'} \right]' + \left[ \frac{\partial(T-U)}{\partial \dot{\phi}} \right]^\bullet - \frac{\partial(T-U)}{\partial \phi} \\ &= (D_\eta - D_\zeta) C_\eta C_\zeta - D_\xi C_\xi' - (I_\eta - I_\zeta) \omega_\eta \omega_\zeta + I_\xi \dot{\omega}_\xi \end{aligned} \quad (3.15)$$

These exact nonlinear expressions have been derived by modifying those equations presented in Ref. [23]. Boundary conditions obtained from terms that were integrated by parts in Eq. (3.8) are as follows:

$$\{D_\xi C_\xi \delta \phi + G_u \delta u + G_v \delta v + G_w \delta w - H_u \delta u' - H_v \delta v' - H_w \delta w'\}_{x=0}^{x=L} = 0 \quad (3.16)$$

where

$$H_\alpha = \left[ \frac{\partial(T-U)}{\partial \psi'} \right] \frac{\partial \psi}{\partial \alpha'} + \left[ \frac{\partial(T-U)}{\partial \theta'} \right] \frac{\partial \theta}{\partial \alpha'} \quad (\alpha = u, v, w) \quad (3.17)$$

The expression for  $\partial \psi / \partial \alpha'$  and  $\partial \theta / \partial \alpha'$  ( $\alpha = u, v, w$ ) in Eqs. (3.9), (3.10) and (3.11) are given as

$$\frac{\partial \psi}{\partial u'} = \frac{-v' \cos^2 \psi}{(1+u')^2} = -\frac{\sin \psi}{\cos \theta} \quad (3.18)$$

$$\frac{\partial \psi}{\partial v'} = \frac{\cos^2 \psi}{1+u'} = \frac{\cos \psi}{\cos \theta} \quad (3.19)$$

$$\frac{\partial \psi}{\partial w'} = 0 \quad (3.20)$$

$$\frac{\partial \theta}{\partial u'} = \frac{w'(1+u') \cos^2 \theta}{[(1+u')^2 + v'^2]^{3/2}} = -\sin \theta \cos \psi \quad (3.21)$$

$$\frac{\partial \theta}{\partial v'} = \frac{v'w' \cos^2 \theta}{[(1+u')^2 + v'^2]^{3/2}} = -\sin \theta \sin \psi \quad (3.22)$$

$$\frac{\partial \theta}{\partial w'} = \frac{\cos^2 \theta}{[(1+u')^2 + v'^2]^{1/2}} = -\cos \theta \quad (3.23)$$

The expressions for  $\dot{\psi}$ ,  $\psi'$ ,  $\dot{\theta}$  and  $\theta'$  are given as:

$$\dot{\psi} = (\dot{v}' \cos \psi - \dot{u}' \sin \psi) \sec \theta \quad (3.24)$$

$$\psi' = (v'' \cos \psi - u'' \sin \psi) \sec \theta \quad (3.25)$$

$$\dot{\theta} = -\dot{w}' \sec \theta \quad (3.26)$$

$$\theta' = -w'' \sec \theta \quad (3.27)$$

where

$$\begin{aligned} u' &= \cos \theta \cos \psi - 1 \\ u'' &= -\frac{v'v'' + w'w''}{1+u'} \\ \dot{u}' &= -\frac{v'\dot{v}' + w'\dot{w}'}{1+u'} \end{aligned}$$

Using Eqs. (3.24)-(3.27) and their derivatives, the expressions for  $C_\xi$ ,  $C_\eta$ ,  $C_\zeta$ ,  $C'_\xi$ ,  $C'_\eta$ ,  $C'_\zeta$  in Eqs. (3.13), (3.14) and (3.15) are obtained. Equation (3.9) together with the boundary condition  $G_u(L, t) = 0$  and the inextensionality constraint given by Eq. (3.5) is used to eliminate  $\lambda$  from the expressions for  $G'_w$  and  $G'_v$ . Thus, integrating Eq. (3.9)

from  $L$  to  $x$  yields

$$\begin{aligned} \int_L^x G'_u dx &= \int_L^x (m\ddot{u} - Q_u) dx \\ \text{or } G_u(x, t) &= \int_L^x (m\ddot{u} - Q_u) dx \end{aligned} \quad (3.28)$$

The Lagrange multiplier,  $\lambda$ , is obtained from Eq. (3.28) as follows:

$$\lambda = \frac{1}{1 + u'} \left[ \int_L^x (m\ddot{u} - Q_u) dx - A_\psi \frac{\partial \psi}{\partial u'} - A_\theta \frac{\partial \theta}{\partial u'} \right] \quad (3.29)$$

Substituting the expression for  $\lambda$  given by Eq. (3.29) in Eqs. (3.10) and (3.11), and using the following simplifications

$$\begin{aligned} \frac{\partial \psi}{\partial v'} - \frac{v'}{1 + u'} \frac{\partial \psi}{\partial u'} &= \frac{1}{\cos \theta \cos \psi} \\ \frac{\partial \theta}{\partial v'} - \frac{v'}{1 + u'} \frac{\partial \theta}{\partial u'} &= 0 \\ \frac{\partial \psi}{\partial w'} - \frac{w'}{1 + u'} \frac{\partial \psi}{\partial u'} &= -\frac{\sin \theta \sin \psi}{\cos^2 \theta \cos \psi} \\ \frac{\partial \theta}{\partial w'} - \frac{w'}{1 + u'} \frac{\partial \theta}{\partial u'} &= -\frac{1}{\cos \theta} \end{aligned} \quad (3.30)$$

the expressions for  $G_v$  and  $G_w$  become

$$G_v = \frac{A_\psi}{\cos \theta \cos \psi} + \frac{v'}{1 + u'} \left[ \int_L^x (m\ddot{u} - Q_u) dx \right] \quad (3.31)$$

$$G_w = -\frac{A_\psi \sin \theta \sin \psi}{\cos^2 \theta \cos \psi} - \frac{A_\theta}{\cos \theta} + \frac{w'}{1 + u'} \left[ \int_L^x (m\ddot{u} - Q_u) dx \right] \quad (3.32)$$

Thus, the governing nonlinear equations for bending-bending-torsion dynamics of a cantilever beam are expressed as:

$$\begin{aligned} m\ddot{v} &= \left\{ \frac{A_\psi}{\cos \theta \cos \psi} + \frac{v'}{1 + u'} \left[ \int_L^x (m\ddot{u} - Q_u) dx \right] \right\}' + Q_v \\ m\ddot{w} &= \left\{ -\frac{A_\psi \sin \theta \sin \psi}{\cos^2 \theta \cos \psi} - \frac{A_\theta}{\cos \theta} + \frac{w'}{1 + u'} \left[ \int_L^x (m\ddot{u} - Q_u) dx \right] \right\}' + Q_w \\ A_\phi &= Q_\phi \end{aligned} \quad (3.33)$$

## 1. Aerodynamics

The load for an airfoil section is given by the quasi-steady aerodynamics as follows,

$$F_A = \pi \rho b^2 V \dot{\phi} + \rho V^2 b C_{L\alpha} (\alpha_{\text{eff}} - c_3 \alpha_{\text{eff}}^3) \quad (3.34)$$

$$M = -\pi \rho b^2 V b \left( \frac{1}{2} - a \right) \dot{\phi} + \rho V^2 b^2 C_{m\alpha} (\alpha_{\text{eff}} - c_3 \alpha_{\text{eff}}^3) \quad (3.35)$$

where  $F_A$  is the aerodynamic force perpendicular to freestream velocity on the airfoil section and  $M$  is the aerodynamic moment. A drag to lift ratio of 0.019 is assumed for the airfoil. A nonlinear parameter  $c_3$  describes the stall nonlinearity. As shown in Eq. (3.34), the stall nonlinearity is expressed by cubic terms. The effective angle of attack  $\alpha_{\text{eff}}$  is defined as follows

$$\alpha_{\text{eff}} = \alpha_0 + \phi - \frac{\dot{v} + V_y}{V} + \frac{b}{V} \left( \frac{1}{2} - a \right) \dot{\phi} \quad (3.36)$$

where  $\alpha_0$  is the root angle of attack and the coefficient  $c_3$  is defined as follows,

$$c_3 = 0.00034189 \left( \frac{180}{\pi} \right)^3 / C_{L\alpha} \quad (3.37)$$

where  $C_{L\alpha} = 2\pi$ . The lift and the drag vector and for each airfoil section can be resolved in the global  $(x, y, z)$  co-ordinate system as shown in Fig. 16. Thus,

$$\begin{bmatrix} Q_u \\ Q_v \\ Q_w \end{bmatrix} = \begin{bmatrix} 0 \\ F_A \cos \alpha_0 + 0.019 F_A \sin \alpha_0 \\ -F_A \sin \alpha_0 + 0.019 F_A \cos \alpha_0 \end{bmatrix} \quad (3.38)$$

Table III. Baseline values of the parameters for the extended heavy Goland wing

Parameter	Value
Semichord, $b$	0.914 $m$ (3 $ft$ )
Wing semispan, $L$	30.48 $m$ (100 $ft$ )
mass per unit span, $m$	538.57 $kg/m$ (11.249 $slug/ft$ )
Out-of-plane bending stiffness, $D_\zeta$	$9.772 \times 10^6 \text{ Nm}^2$ ( $23.647 \times 10^6 \text{ lb ft}^2$ )
In-plane bending stiffness, $D_\eta$	$1.4072 \times 10^9 \text{ Nm}^2$ ( $34.052 \times 10^8 \text{ lb ft}^2$ )
Torsional stiffness, $D_\xi$	$9.871 \times 10^5 \text{ Nm}^2$ ( $2.3899 \times 10^6 \text{ lb ft}^2$ )
Pitch inertia, $I_\xi$	111.955 $kg m$ (25.17 $slug ft$ )
Elastic axis,	0.6096 $m$ (2 $ft$ ) from leading edge
Centroidal axis	0.792 $m$ (2.6 $ft$ ) from leading edge

## B. Dynamics about Nonzero Equilibria

The solution procedure is same as that elaborated in chapter II. A balance of total lift and weight is assumed. This constraint can be expressed mathematically as

$$\rho(V_\infty^2 + V_y^2)bC_{L_\alpha}\alpha_0L = mgL + M_0g$$

$$\alpha_0 = \frac{(mL + M_0)g}{\rho(V_\infty^2 + V_y^2)bC_{L_\alpha}L}$$

The balance of pitching moment is also assumed and is generally attained through tail and elevator which have not been modeled in this analysis.

The extended heavy Goland wing with parameters shown in Table III has been used as the baseline configuration. The wing semi-span of original heavy Goland wing[17] has been changed to 100 feet resulting in an aspect ratio of approximately 33 for a cantilevered semispan wing. Figure 17 shows the out-of-plane modal coordinate



equilibria and limit cycles as the freestream velocity is varied. The spanwise location of this response is approximately at midspan. The thin solid line represents stable equilibria. The thin broken line represents unstable equilibria. The thick solid line represents the amplitude of stable LCOs. This notation is followed for all results presented here.

The wing in the left view of Fig. 17 has a root angle of attack of zero. The system loses stability at a velocity of approximately 60 ft/sec. This is a typical flutter velocity of uniform cantilevered wing with static equilibria of zero. A Hopf bifurcation (represented by a cross symbol) occurs at this velocity. LCOs originate at Hopf bifurcations. For velocities greater than this velocity, the system undergoes LCOs with amplitudes shown in Fig. 17. If the trim condition is such that  $\alpha_0 = 2.8^\circ$ , the system characteristics changes. As expected, the static deformed shape of the wing varies as the freestream velocity is varied. The out-of-plane modal coordinate has been shown in Fig. 17. The static deformation increases with increasing freestream velocity. The dynamic instability occurs at a velocity higher than the case with zero equilibria. The result in Fig. 17 is corroborated by numerical simulation. Figure 18 shows system response for the two different root angles of attack under consideration at a freestream velocity,  $V = 70$  ft/sec. This velocity is higher than flutter velocity ( $V_F = 60$  ft/sec) for the  $\alpha_0 = 0^\circ$  case. As shown in the bifurcation diagrams, the system settles into LCOs for  $\alpha_0 = 0^\circ$ . The amplitude of oscillation is consistent with Fig. 17(a). However, with  $\alpha_0 = 2.8^\circ$ , the wing undergoes a static deformation as seen in Fig. 18(b). The value of the non-zero deformation is again consistent with Fig. 17(b).

### 1. Stiffness Ratio Effect

The locus of Hopf bifurcation in Fig. 17 is extended to  $V$ - $\beta_\eta$  parameter space by two parameter continuation method. This loci of bifurcation are illustrated in Fig. 19. As the stiffness ratio,  $\beta_\eta$  is decreased the stability threshold velocity decreases gradually. The boundary shifts upward for increasing value of  $\alpha_0$ . There is a sharp increase in threshold velocity for values of  $\beta_\eta < 20$ . Thus, the stiffness ratio cast an important influence on the stability threshold for nonzero equilibrias. Figure 20 compares bifurcation diagram for two different values of  $\beta_\eta$ . The left view shows in-plane modal response for  $\beta_\eta = 25$  and the right view shows the same for  $\beta_\eta = 144$ . The flutter velocity for  $\beta_\eta = 25$  is approximately 25% lower than that for  $\beta_\eta = 144$ . Also, the amplitude of LCO for  $\beta_\eta = 25$  is higher than that for  $\beta_\eta = 144$ .

Figure 21 shows the locus of eigenvalues as the velocity is varied for the two values of  $\beta_\eta$ . The Jacobian matrix is generated by the continuation tool at each point of the bifurcation diagram in Fig. 20 by performing a linearization about the nonlinear equilibria. The eigenvalues shown in Fig. 21 are extracted from these Jacobian matrices. The stability of the system requires all the eigenvalues to be located in the left half complex plane. A Hopf bifurcation occurs whenever a complex pair of eigenvalues crosses the imaginary axis. The eigenvalues associated with the in-plane, out-of-plane and torsion modes have been identified. The instability for  $\beta_\eta = 144$  is associated with the torsion mode; however, the instability for  $\beta_\eta = 25$  is associated with the in-plane mode. Thus, modeling of the in-plane degree of freedom is important to characterize the dynamic stability of the system, specially at lower values of stiffness ratios. This point is further illustrated by Fig. 22 which compares bifurcation diagrams for two different systems. The left view shows characteristics of system with a linear structure model. The in-plane degree of freedom has been excluded here.

Table IV. Subcritical bifurcation

$\beta_\eta$	AR	Subcritical
2	33	Yes
4	33	No
4	40	Yes
2	40	Yes
2	27	No
1.5	27	No
1.2	27	Yes

The right view shows the bifurcation characteristics of the system with all structural nonlinearities, including those due to in-plane degree of freedom. The locus of eigenvalues for this system has been shown in Fig. 21(a). The dynamic instability for the linear system occurs at a velocity higher than the system with nonlinear structural model. The instability is associated with the torsion mode unlike the former system. Thus, the exclusion of in-plane motion in the modeling can result in over prediction of the system's stability boundary.

## 2. Subcritical Hopf Bifurcation

Subcritical bifurcations are of particular interest. LCO states may exist for velocities lower than the conventional flutter velocity. The dynamics of the system within a range of velocity below flutter velocity is governed by the size of the initial condition. For sufficiently large enough initial conditions, the system becomes entrained in LCOs. Stable dynamics are exhibited for small initial conditions. Once the system is trapped in an LCO, the velocity must be decreased to a value much lower than flutter velocity

to recover.

We showed in our earlier research[20] that the structural nonlinearity plays a role in inducing subcritical bifurcations. Here in, our work explores this phenomenon further with an attempt to ascertain the effect of various system parameters in inducing subcritical bifurcations. Figure 23 compares bifurcation diagrams of the out-of-plane modal responses for different stiffness ratios. Bifurcation diagrams for three different stiffness ratio is illustrated. Although an increase in flutter velocity is seen with a decrease in stiffness ratio, this behavior is offset by the subcritical LCO branch. Figure 24 shows the bifurcation diagram with in-plane modal response. The amplitude of in-plane subcritical LCOs tend to increase with decreasing stiffness ratio. Thus, in-plane degree of freedom becomes increasingly important for lower stiffness ratio. Simulation results confirm the subcritical nature of the system. Figure 25 and 26 shows the results of simulations for two different initial condition for a system with subcritical characteristics. Stable dynamics are seen for low initial conditions and LCO is seen for large initial condition. Table IV summarizes the bifurcations characteristics of system for several combinations of aspect ratio and stiffness ratios. It can be deduced that the system tends to become subcritical with decreasing stiffness ratio and increasing aspect ratio. The influence of aspect ratio is illustrated in Fig. 27. For a given stiffness ratio, the system goes from supercritical to subcritical with an increase in aspect ratio.

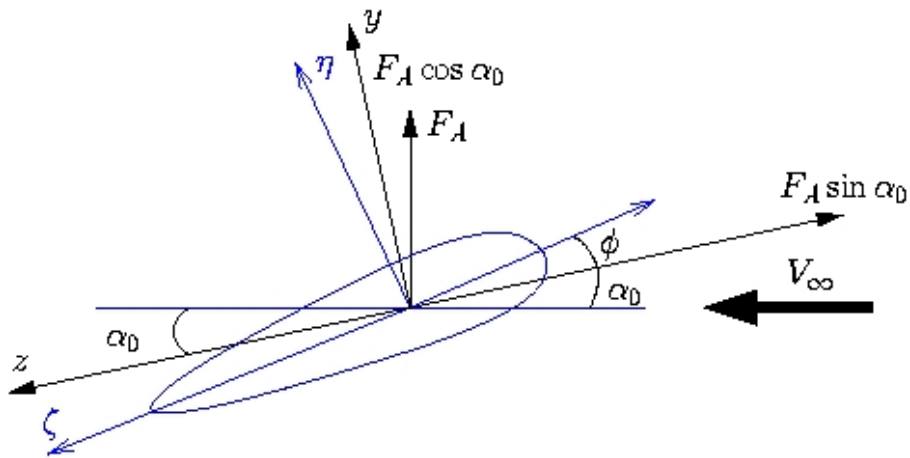
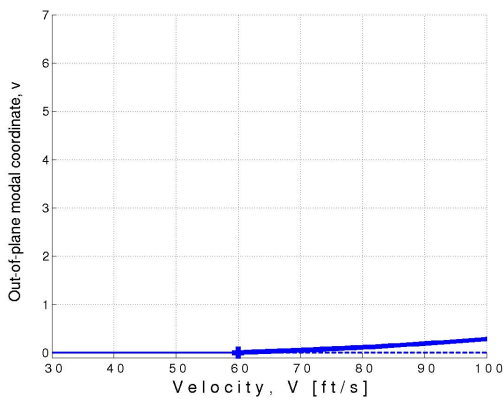
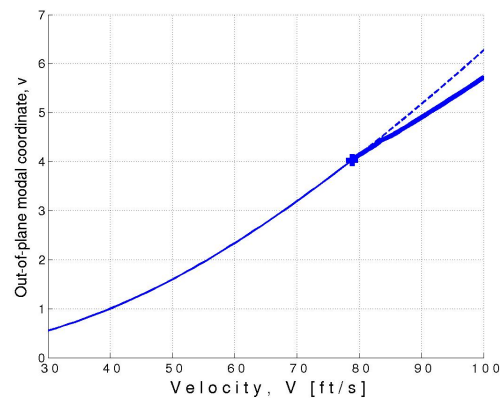


Fig. 16. Airfoil section showing the lift resolved in  $(x, y, z)$  coordinate system

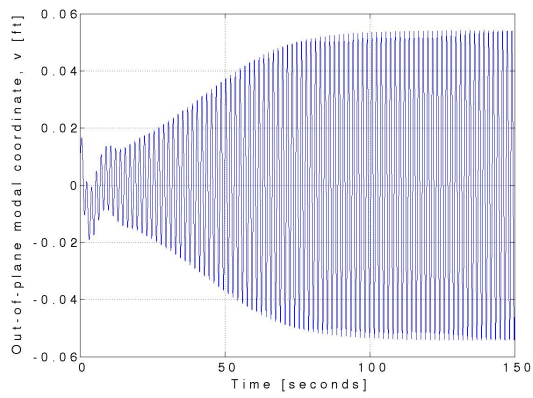
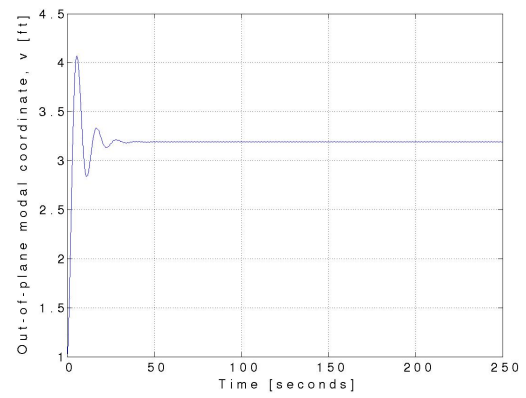


(a)  $\alpha_0 = 0.0^\circ$



(b)  $\alpha_0 = 2.8^\circ$

Fig. 17. Bifurcation diagram with  $V$  as the parameter showing the out-of-plane bending modal coordinate for the heavy Goland wing with  $L=100$ ,  $\beta_\eta = 144$  for two different root angles of attack,  $\alpha_0$

(a)  $\alpha_0 = 0.0^\circ$ (b)  $\alpha_0 = 2.8^\circ$ Fig. 18. Simulation result at  $V=70$  ft/s for two different root angles of attack

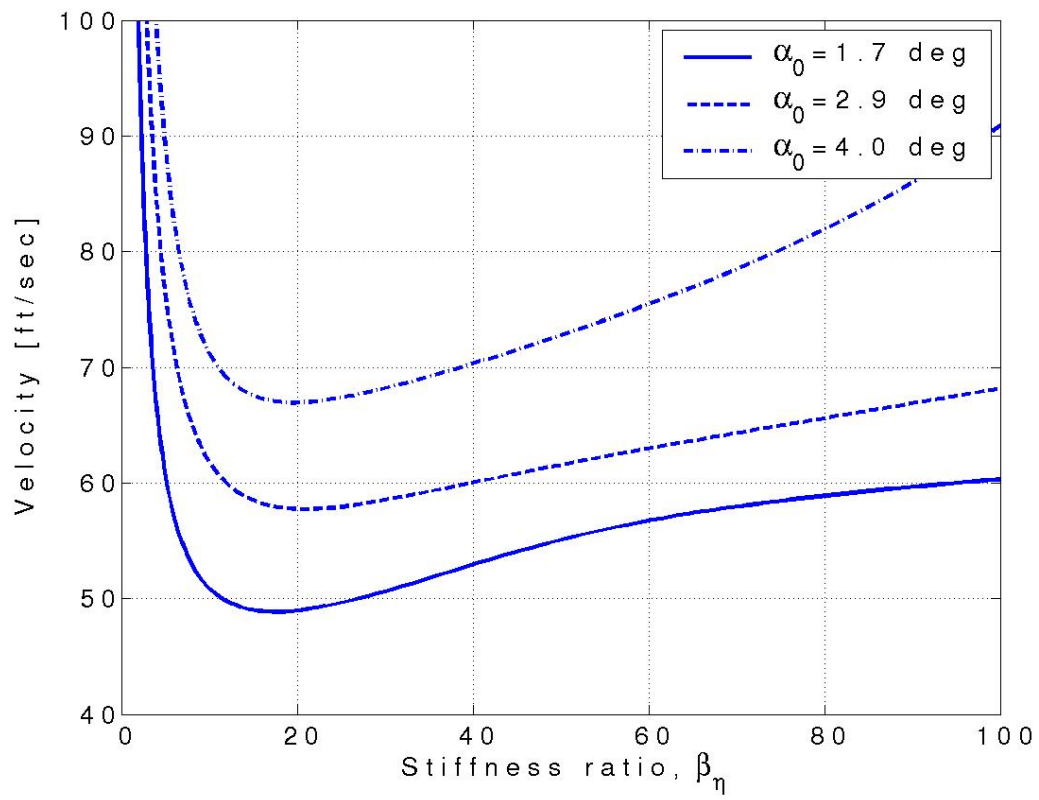


Fig. 19. Locus of Hopf bifurcation in  $V$ - $\beta_\eta$  parameter space for various values of  $\alpha_0$

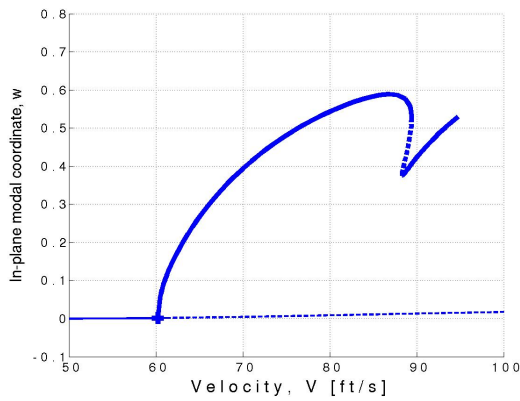
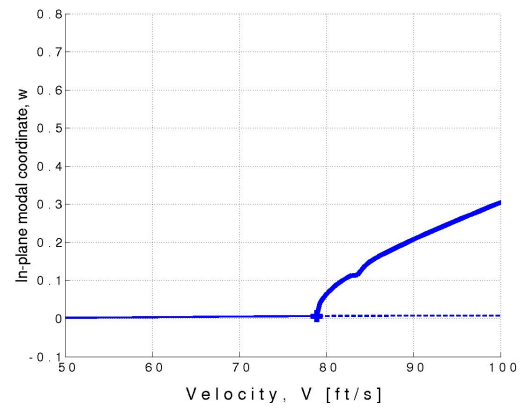
(a)  $\beta_\eta = 25$ (b)  $\beta_\eta = 144$ 

Fig. 20. Bifurcation diagram with  $V$  as the parameter showing the in-plane bending modal coordinate for the heavy Goland wing with  $L=100$ ,  $\alpha_0 = 2.8^\circ$  for two different stiffness ratios,  $\beta_\eta$

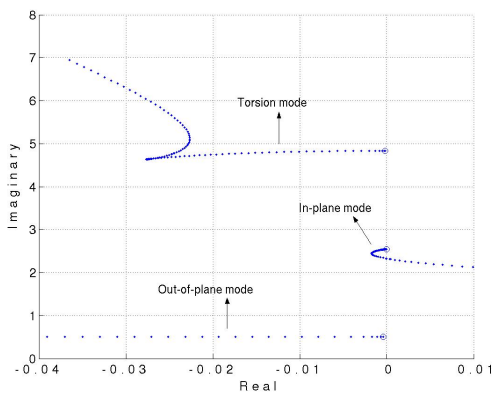
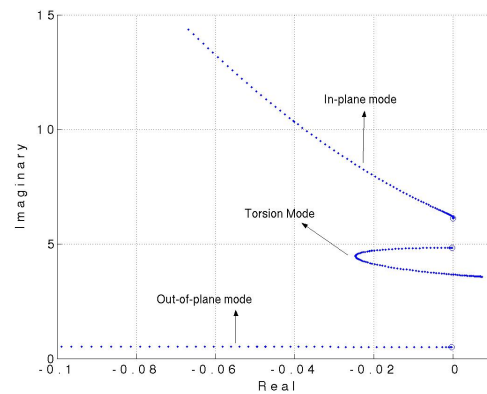
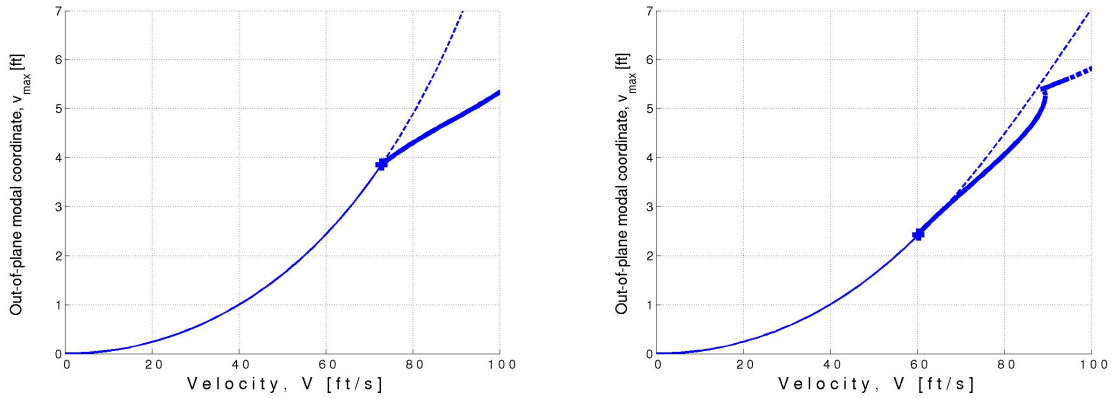
(a)  $\beta_\eta = 25$ (b)  $\beta_\eta = 144$ 

Fig. 21. Locus of eigenvalues for different values of stiffness ratio

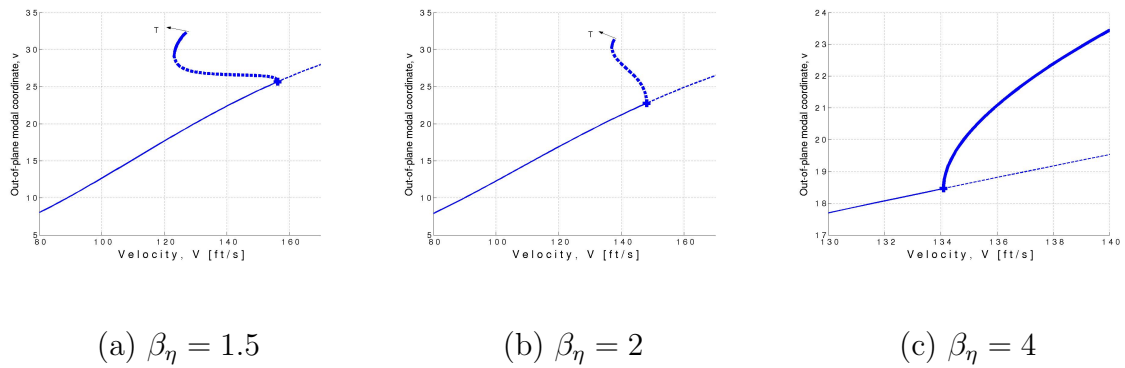




(a) Linear structure without in-plane degree of freedom

(b) Nonlinear structure with in-plane degree of freedom included

Fig. 22. Comparison of bifurcation diagrams with  $V$  as the parameter showing the out-of-plane bending modal coordinate for the heavy Goland wing with  $\beta_\eta = 25$ ,  $L = 100$  and  $\alpha_0 = 2.8^\circ$



(a)  $\beta_\eta = 1.5$

(b)  $\beta_\eta = 2$

(c)  $\beta_\eta = 4$

Fig. 23. Comparison of bifurcation diagrams with  $V$  as the parameter showing the out-of-plane bending modal coordinate for the heavy Goland wing with  $L = 100$  and  $\alpha_0 = 5.6^\circ$

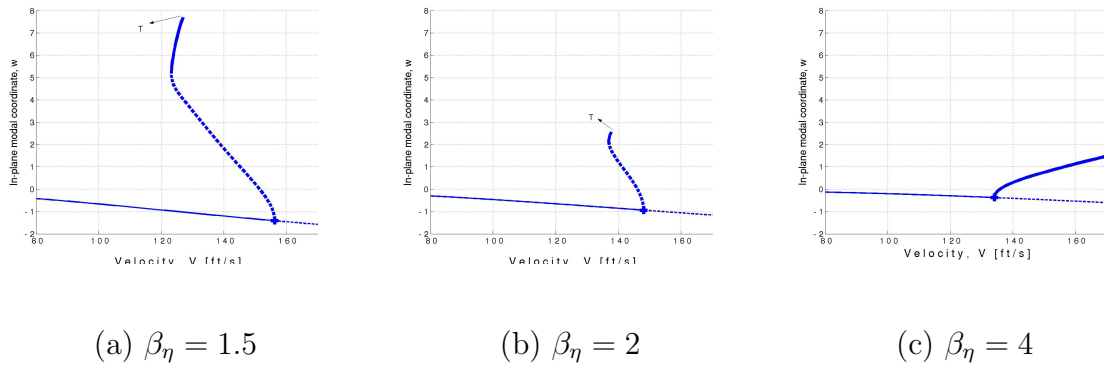
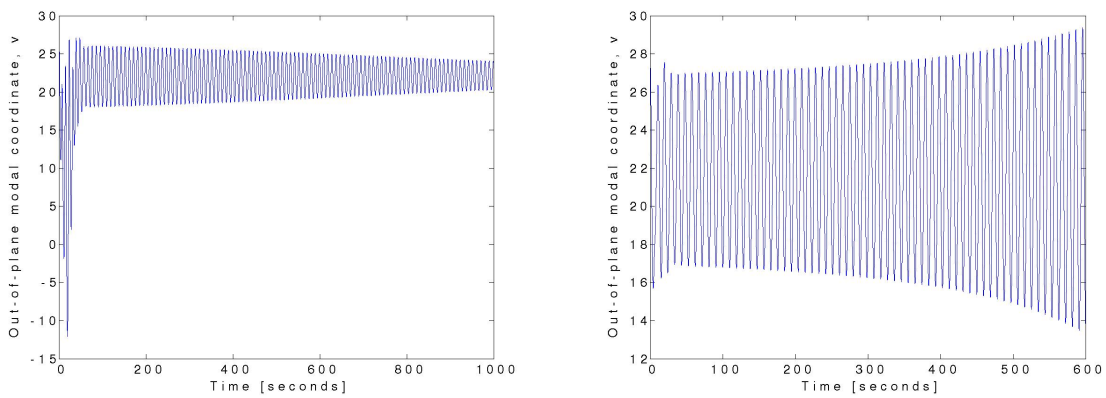
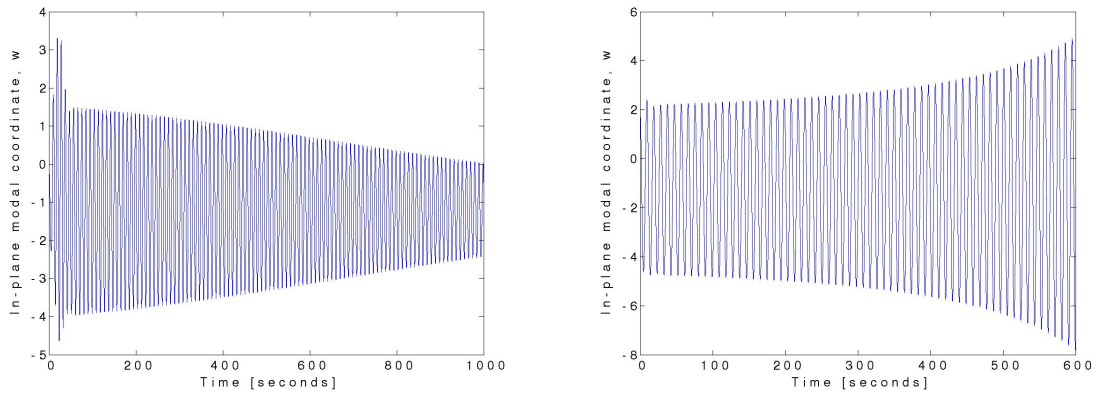


Fig. 24. Comparison of bifurcation diagrams with  $V$  as the parameter showing the in-plane bending modal coordinate for the heavy Goland wing with  $L = 100$  and  $\alpha_0 = 5.6^\circ$



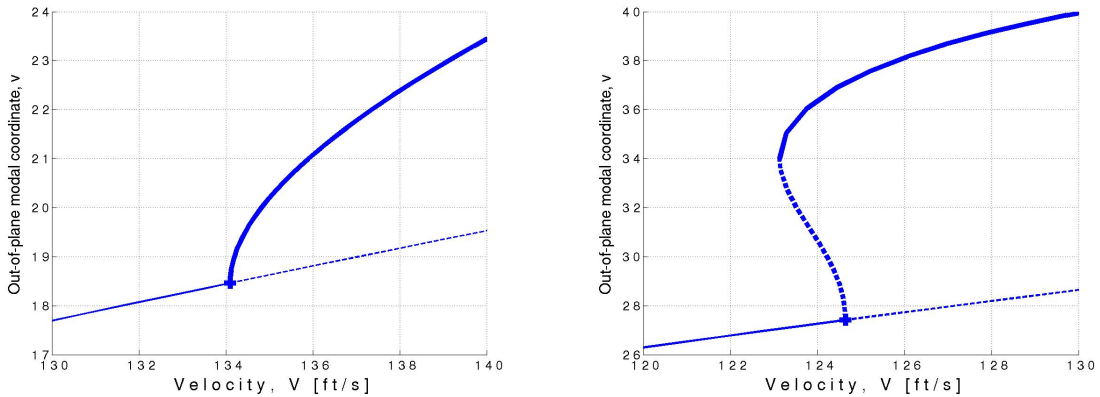
(a)  $(w_0, v_0, \phi_0, \dot{w}_0, \dot{v}_0, \dot{\phi}_0) = (0, 28, 0.08, 0, 0, 0)$  (b)  $(w_0, v_0, \phi_0, \dot{w}_0, \dot{v}_0, \dot{\phi}_0) = (2, 28, 0.08, 0, 0, 0)$

Fig. 25. Out-of-plane bending response and two different initial conditions for  $V = 140$  ft/sec,  $\beta_\eta = 25$ ,  $L = 100$  feet and  $\alpha_0 = 2.8^\circ$



(a)  $(w_0, v_0, \phi_0, \dot{w}_0, \dot{v}_0, \dot{\phi}_0) = (0, 28, 0.08, 0, 0, 0)$  (b)  $(w_0, v_0, \phi_0, \dot{w}_0, \dot{v}_0, \dot{\phi}_0) = (2, 28, 0.08, 0, 0, 0)$

Fig. 26. In-plane bending response and two different initial conditions for  $V = 140$  ft/sec,  $\beta_\eta = 25$ ,  $L = 100$  feet and  $\alpha_0 = 2.8^\circ$



(a)  $AR = 33$

(b)  $AR = 40$

Fig. 27. Comparison of bifurcation diagrams with  $V$  as the parameter showing the out-of-plane bending modal coordinate with  $\beta_\eta = 4$  and  $\alpha_0 = 2.8^\circ$

## CHAPTER IV

### CONCLUSIONS

Two different nonlinear formulations for bending-bending-torsion dynamics of cantilevered wing was presented. The first formulation considers large amplitude vibration of a wing about zero undeformed equilibria. This formulation was used to investigate the effects of structural nonlinearities on the bifurcation characteristics of the system. A two is to one type internal resonance leading to large amplitude in-plane motion was demonstrated using this model. Later, a physical model which did not have limitation of zero equilibria was presented. Dynamics about nonzero trim states was investigated for using this model. Kinematic nonlinearities due to curvature and inertia was retained in their exact form. This nonlinear formulation permitted the analysis of dynamics about nonzero trims as the model does not require a priori assumption about the static trim shape of the wing. A continuation algorithm applied to this formulation facilitated the computation of nonzero trims as a system parameter was varied. This represents direct method for eigenanalysis of aeroelastic system. The method automated the computation of trim states and their stability. The parameter space related to design was investigated for stability characteristics. Stiffness ratio and aspect ratio were found to be the two most important parameter affecting the design. The in-plane degree of freedom begins to participate in the dynamics instability phenomenon at low stiffness ratios. Eigenanalysis revealed that the instability at low stiffness ratio configuration is related to in-plane mode. Thus, the modeling of in-plane degree of freedom is necessitated for low stiffness ratio configuration. Low stiffness ratio configuration also rendered the system more prone to subcritical LCOs. In general, subcritical bifurcation was found to be more likely for low stiffness ratio and high aspect ratio configurations.

## REFERENCES

- [1] R. W. Bunton and C. M. Denegri Jr., “Limit Cycle Oscillation Characteristics of Fighter Aircraft,” *Journal of Aircraft*, vol. 37, no. 5, pp. 916–918, 2000.
- [2] C. M. Denegri Jr., “Limit Cycle Oscillation Flight Test Results of a Fighter with External Stores,” *Journal of Aircraft*, vol. 37, no. 5, pp. 761–769, 2000.
- [3] K. Kim and T. W. Strganac, “Nonlinear Responses of a Cantilever Wing with an External Store,” in *44th AIAA Structures, Structural Dynamics, and Materials Conference*, Norfolk, VA, 2003, AIAA Paper 2003-1708.
- [4] K. Kim, C. Nickkawde and T. W. Strganac, “Effect of External Store on Non-linear Aeroelastic Responses,” in *45th AIAA Structures, Structural Dynamics, and Materials Conference*, Palm Springs, CA, 2004, AIAA Paper 2004-1942.
- [5] P. S. Beran, T. W. Strganac, K. Kim and C. Nickkawde, “Store Induced Limit Cycle Oscillations Using a Model with Full System Nonlinearities,” *Nonlinear Dynamics*, vol. 37, no. 4, pp. 323–339, 2004.
- [6] M. R. M. Crespo da Silva and C. G. Glynn, “Nonlinear Flexural-Flexural-Torsional Dynamics of Inextensional Beams. I Equations of Motion,” *Journal of Structural Mechanics*, vol. 6, no. 4, pp. 437–448, 1978.
- [7] K. Kim, “Nonlinear Aeroelastic Analysis of Aircraft Wing-with-Store Configurations,” Ph.D. dissertation, Texas A&M University, College Station, TX, 2004.
- [8] M. R. M. Crespo da Silva, “Non-linear Flexural-Flexural-Torsional-Extensional Dynamics of Beams-I. Formulation,” *International Journal of Solids and Structures*, vol. 24, no. 12, pp. 1225–1234, 1988.

- [9] B. Carnahan, H. A. Luther and J. O. Wilkes, *Applied Numerical Methods*, New York: John Wiley & Sons, pp. 361–365 .
- [10] E. J. Doedel, "AUTO: A Program for the Automatic Bifurcation Analysis of Autonomous Systems," in *Proceedings of the 10th Manitoba Conference on Numerical Mathematics and Computations*, University of Manitoba, Winnipeg, Canada, 1981, pp. 265–284.
- [11] R. Seydel, *Practical Bifurcation and Stability Analysis - From Equilibrium to Chaos*, Interdisciplinary Applied Mathematics 5, New York: Springer-Verlag, 1994.
- [12] E. L. Allgower and K. Geog, *Numerical Continuation Methods*, New York: Springer-Verlag, 1990.
- [13] E. J. Doedel, R. C. Paffenroth, A. R. Champneys, T. F. Fairgrieve, Y. A. Kuznetsov, B. Sandstede and X. J. Wang, "AUTO2000: Continuation and Bifurcation Software for Ordinary Differential Equations", Technical Report, California Institute of Technology, 2002.
- [14] A. H. Nayfeh and D. T. Mook, *Nonlinear Oscillation*, New York: Wiley, 1979.
- [15] K. L. Tuer, M. F. Golnaraghi and D. Wang, "Development of a Generalized Active Vibration Suppression Strategy for a Cantilever Beam Using Internal Resonance," *Nonlinear Dynamics*, vol. 5, pp. 131–151, 1994.
- [16] A. H. Nayfeh and B. Balachandran, "Modal Interactions in Dynamical and Structural Systems," *Applied Mechanics Review*, vol. 42, no. 11, part 2, pp. S175–S201, 1989.

- [17] F. E. Eastep, “Transonic Flutter Analysis of a Rectangular Wing with Conventional Airfoil Sections,” *AIAA Journal*, vol. 18, no. 10, pp. 1159–1164, 1980.
- [18] M. J. Patil and D. H. Hodges, “Flight Dynamics of Highly Flexible Flying Wings,” in *Proceedings of the International Forum on Aeroelasticity and Structural Dynamics*, Munich, Germany, June 2005.
- [19] M. J. Patil, D. H. Hodges and C. E. S. Cesnik, “Nonlinear Aeroelasticity and Flight Dynamics of High-Altitude Long-Endurance Aircraft,” *Journal of Aircraft*, vol. 38, no. 1, pp. 88–94, 2001.
- [20] T. W. Strganac, P. G. Cizmas, C. Nickkawde, J. I. Gargaloff and P. S. Beran, “Aeroelastic Analysis of Future Air Vehicles Concept Using a Fully Nonlinear Methodology,” in *46th AIAA Structures, Structural Dynamics, and Materials Conference*, Austin, TX, 2005, AIAA Paper 2005-2171.
- [21] P. F. Pai and A. H. Nayfeh, “Three Dimensional Nonlinear Vibration of Composite Beams-I: Equations of Motion,” *Nonlinear Dynamics*, vol. 1, pp. 477–502, 1990.
- [22] H. Schaub and J. L. Junkins, *Analytical Mechanics of Space System*, Reston, VA: AIAA Education Series, 2003.
- [23] M. R. M. Crespo da Silva, “Equations for Nonlinear Analysis of 3D Motions of Beam,” *Applied Mechanics Review*, vol. 44, no. 1, part 2, pp. S51–S59, Nov 1991.

## APPENDIX A

MODELING OF A FLEXIBLE WING WITH LONGITUDINAL RIGID BODY  
DEGREE OF FREEDOM

Equations of motions of flying flexible wing with rigid body pitch and plunge degree of freedom is derived in this appendix. These equations would be useful for future research involving analysis of nonlinear coupling between flexible body modes and longitudinal flight dynamics modes. Structural coupling terms between rigid body and flexible body term is retained upto second order. The angular velocity of any point on the cantilevered wing is given by:

$$\vec{\omega} = \mathbf{M}_{\text{rot}} \times \vec{\omega}_B + \vec{\omega}_s \quad (\text{A.1})$$

where

$$\vec{\omega}_B = \dot{\alpha} \hat{x}$$

$$\vec{\omega}_s = (\dot{\phi} - \dot{\psi} \sin \theta) \hat{\xi} + (\dot{\psi} \cos \theta \sin \phi + \dot{\theta} \cos \phi) \hat{\eta} + (\dot{\psi} \cos \theta \cos \phi - \dot{\theta} \sin \phi) \hat{\zeta}$$

and

$$\mathbf{M}_{\text{rot}}(\mathbf{s}, \mathbf{t}) = \begin{bmatrix} \cos(\theta) \cos(\psi) & \cos(\theta) \sin(\psi) & -\sin(\theta) \\ -\cos(\phi) \sin(\psi) + \sin(\phi) \sin(\theta) \cos(\psi) & \cos(\phi) \cos(\psi) + \sin(\phi) \sin(\theta) \sin(\psi) & \sin(\phi) \cos(\theta) \\ \sin(\phi) \sin(\psi) + \cos(\phi) \sin(\theta) \cos(\psi) & -\sin(\phi) \cos(\psi) + \cos(\phi) \sin(\theta) \sin(\psi) & \cos(\phi) \cos(\theta) \end{bmatrix}$$

Retaining terms upto second order in  $\alpha$ ,

$$\begin{aligned} \vec{\omega} &= (\dot{\phi} - \dot{\psi} \sin \theta + \dot{\alpha}) \hat{\xi} + (\dot{\psi} \cos \theta \sin \phi + \dot{\theta} \cos \phi - \psi \dot{\alpha}) \hat{\eta} \\ &\quad + (\dot{\psi} \cos \theta \cos \phi - \dot{\theta} \sin \phi + \theta \dot{\alpha}) \hat{\zeta} \\ &= (\omega_\xi + \dot{\alpha}) \hat{\xi} + (\omega_\eta - \dot{\alpha} \psi) \hat{\eta} + (\omega_\zeta + \dot{\alpha} \theta) \hat{\zeta} \end{aligned} \quad (\text{A.2})$$

The velocity vector in  $(x, y, z)$  coordinate system is given as:

$$\vec{V} = \dot{u} \hat{x} + (\dot{v} + V_\infty \sin \alpha + V_y \cos \alpha) \hat{y} + (\dot{w} + V_\infty \cos \alpha - V_y \sin \alpha) \hat{z}$$



The total kinetic energy of the system is given by

$$T_{tot} = \int_0^L \left( \frac{1}{2} m (\dot{u}^2 + (\dot{v} + V_\infty \sin \alpha + V_y \cos \alpha)^2 + (\dot{w} + V_\infty \cos \alpha - V_y \sin \alpha)^2) dx \right. \\ \left. + \int_0^L \frac{1}{2} (I_\xi (\omega_\xi + \dot{\alpha})^2 + I_\eta (\omega_\eta - \dot{\alpha} \psi)^2 + I_\zeta (\omega_\zeta + \dot{\alpha} \theta)^2) dx \right) \quad (\text{A.3})$$

$V_y$  and  $V_\infty$  are rigid body velocities in  $y$  and  $z$  directions respectively.  $V_\infty$  is the freestream velocity and is assumed to be constant in straight and level flight.  $V_y$  is the perturbation in freestream velocity in vertical  $y$  direction. The potential energy for the system is given by Eq. (3.7). The rigid body plunge motion equation is given by:

$$\frac{D}{Dt} \left( \frac{\partial T_{tot}}{\partial V_y} \right) = \int_0^L F_A dx - mLg \\ mL(\dot{V}_y) = - \int_0^L m (\ddot{v} \cos \alpha - \ddot{w} \sin \alpha) dx \\ + \int_0^L m \dot{\alpha} (\dot{v} \sin \alpha + \dot{w} \cos \alpha) dx + \int_0^L F_A dx - mLg \quad (\text{A.4})$$

The rigid body pitch degree of freedom equation is obtained as:

$$\left[ \frac{\partial(T_{tot} - U)}{\partial \dot{\alpha}} \right]^\bullet - \frac{\partial(T_{tot} - U)}{\partial \alpha} = \int_0^L M \cos(\theta) \cos(\psi) dx$$

Thus, the equation of motion is given by:

$$\int_0^L I_\xi (\ddot{\alpha} + \ddot{\phi}) dx = \int_0^L m \dot{w} (V_\infty \sin \alpha + V_y \cos \alpha) dx \\ - \int_0^L m \dot{v} (V_\infty \cos \alpha - V_y \sin \alpha) dx \\ + \int_0^L ((I_\xi - I_\zeta)(\theta \ddot{\psi} + \dot{\theta} \dot{\psi}) + I_\eta (\ddot{\theta} \psi + \dot{\theta} \dot{\psi})) dx \\ + \int_0^L M \cos(\theta) \cos(\psi) dx \quad (\text{A.5})$$

$A_\phi$ ,  $A_\theta$  and  $A_\psi$  are now given as:

$$A_\psi = \{D_\xi C_\xi \sin \theta - (D_\eta C_\eta \sin \phi + D_\zeta C_\zeta \cos \phi) \cos \theta\}'$$

$$\begin{aligned}
& + [(I_\eta \omega_\eta \sin \phi + I_\zeta \omega_\zeta \cos \phi) \cos \theta - I_\xi \omega_\xi \sin \theta]^\bullet \\
& - (I_\xi - I_\zeta)(\ddot{\alpha}\theta + \dot{\alpha}\dot{\theta}) + I_\eta \dot{\alpha}\dot{\theta}
\end{aligned}$$

$$\begin{aligned}
A_\theta & = (D_\zeta C_\zeta \sin \phi - D_\eta C_\eta \cos \phi)' \\
& - (D_\eta C_\eta \sin \phi + D_\zeta C_\zeta \cos \phi) \psi' \sin \theta - D_\xi C_\xi \psi' \cos \theta \\
& - (I_\zeta \omega_\zeta \sin \phi - I_\eta \omega_\eta \cos \phi)^\bullet + (I_\eta \omega_\eta \sin \phi + I_\zeta \omega_\zeta \cos \phi) \dot{\psi} \sin \theta \\
& + I_\xi \omega_\xi \dot{\psi} \cos \theta + (I_\xi - I_\zeta) \dot{\alpha} \dot{\psi} - I_\eta (\ddot{\alpha} \psi + 2 \dot{\alpha} \dot{\psi})
\end{aligned}$$

$$A_\phi = (D_\eta - D_\zeta) C_\eta C_\zeta - D_\xi C'_\xi - (I_\eta - I_\zeta) \omega_\eta \omega_\zeta + I_\xi \dot{\omega}_\xi + I_\xi \ddot{\alpha}$$

The structural equations of motions are given as:

$$\begin{aligned}
& m (\ddot{v} + \dot{V}_y \cos \alpha - V_y \dot{\alpha} \sin \alpha + V_\infty \dot{\alpha} \cos \alpha) \\
& = \left\{ \frac{A_\psi}{\cos \theta \cos \psi} + \frac{v'}{1 + u'} \left[ \int_L^x (m\ddot{u} - Q_u) dx \right] \right\}' + Q_v - mg \tag{A.6}
\end{aligned}$$

$$\begin{aligned}
& m (\ddot{w} - \dot{V}_y \sin \alpha - V_y \dot{\alpha} \cos \alpha - V_\infty \dot{\alpha} \sin \alpha) \\
& = \left\{ -\frac{A_\psi \sin \theta \sin \psi}{\cos^2 \theta \cos \psi} - \frac{A_\theta}{\cos \theta} + \frac{w'}{1 + u'} \left[ \int_L^x (m\ddot{u} - Q_u) dx \right] \right\}' + Q_w \tag{A.7}
\end{aligned}$$

$$A_\phi = M \tag{A.8}$$

Equations (A.4) and (A.5) together with Eqs. (A.6), (A.7) and (A.8) are the coupled equations of motion for a flexible wing with longitudinal rigid body degree of freedom.

## VITA

Chetan Nichkawde was born in India. He is the first and only son of Suresh P. Nichkawade and Asha Nichkawde. He attended Delhi Public School, Dhanbad. He obtained his Bachelor of Technology degree in Aerospace Engineering from Indian Institute of Technology Bombay in 2003. He simultaneously obtained Master of Technology degree in Control and Guidance under dual degree program from Indian Institute of Technology Bombay. He has served as Graduate Research Assistant at Texas A&M University since September of 2003. His interest lies in the broad area of Control and Dynamical Systems. He intends to evolve into a technologist and entrepreneur in this area.

His permanent address is:

XI/B-68, Koylanagar

Dhanbad - 826005

Jharkhand, INDIA

The typist for this thesis was Chetan Nichkawde.